THESIS FOR THE DEGREE OF LICENTIATE OF ENGINEERING

Kinetic Studies of NO Oxidation and Reduction over Silver-Alumina Catalyst

MUHAMMAD MUFTI AZIS

Department of Chemical and Biological Engineering

CHALMERS UNIVERSITY OF TECHNOLOGY

Göteborg, Sweden 2013

Kinetic Studies of NO Oxidation and Reduction over Silver-Alumina Catalyst
Muhammad Mufti Azis

Licentiatuppsatser vid Institutionen för Kemi- och bioteknik
Chalmers tekniska högskola
Serie nr. 2013: 17
ISSN 1652-943X

Department of Chemical and Biological Engineering
Chalmers University of Technology
SE-41296 Göteborg, Sweden
Telephone: +4631 7721000

Printed by:
Reproservice
Göteborg, Sweden (2013)

Kinetic Studies of NO Oxidation and Reduction over Silver-Alumina Catalyst

MUHAMMAD MUFTI AZIS
Department of Chemical and Biological Engineering
Chalmers University of Technology, Göteborg 2013

Abstract

In line with growing concerns to manufacture more environmentally friendly vehicles, the use of internal combustion engines operating with oxygen excess or so called lean-burn engines will continue to be increasingly used. For lean-burn operation, reduction of NOx ($NO+NO_2$) emissions is a major challenge and it is therefore urgently required to develop efficient and reliable NOx reduction aftertreatment systems for a wide variety of lean-burn or diesel engines. The main goal of this thesis is to increase the understanding of the reaction mechanism of selective catalytic reduction (SCR) of NOx with a hydrocarbon (HC) reductant over Ag-Al_2O_3 catalysts.

As an important subsystem in the HC-SCR mechanism, H_2 assisted NO oxidation over a monolith-supported Ag-Al_2O_3 catalyst was investigated by constructing a microkinetic model that accounted for heat and mass transport in the catalyst washcoat. The effect of H_2 examined in the kinetic model, was to reduce self-inhibiting surface nitrate species on active sites. A reduced factorial design of the inlet experimental conditions was used to generate transient experimental data. In general, the modelling results could reproduce the transient experimental data well with correct levels of outlet concentrations and time scales for transient responses. When H_2 was present in the feed, the kinetic model showed that H_2 was consumed rapidly in the front part of the monolith. This indicated that the H_2 promotion of the NO oxidation reaction may have been isolated to only a portion of the catalyst.

A series of temperature-programmed desorption (TPD) studies of NOx were conducted over Ag-Al_2O_3 catalysts to quantify and characterize the stability of surface NOx species. Formation of two general groups of surface NOx species were found to be present: a less thermally stable group of so called “low temperature (LT) nitrates” and a more thermally stable group of “high temperature (HT) nitrates”. The LT NOx desorption peak could be attributed to the decomposition of nitrate species formed on the active sites. Elimination or decrease in quantities of these LT nitrates either thermally or by reaction with H_2 resulted in higher NO oxidation and NOx reduction conversion. The HT NOx desorption peak primarily corresponded to the decomposition of nitrates on the Al_2O_3 support and could be considered spectator surface species. It was also found that H_2 facilitates formation of nitrate on the Al_2O_3 support and it was indicative that the mechanism of NOx storage on the Al_2O_3 support was mainly via NO_2 readsorption. From TPD studies of C_3H_6-SCR in the presence and absence of H_2, it was shown that the presence of H_2 not only eliminated LT nitrates but also promoted the formation of adsorbed hydrocarbons. Therefore, the dual role of H_2 to both eliminate nitrates from active sites and promote NOx storage was elucidated.

Keywords: HC-SCR, Silver Alumina, Hydrogen effect, Kinetic modeling, TPD, NOx reduction, NO oxidation.

List of Appended Papers

This work is based on the work presented in the following papers:

I. **Microkinetic modeling of H_2-assisted NO oxidation over $Ag\text{-}Al_2O_3$**
Muhammad Mufti Azis, Hanna Härelind, Derek Creaser
Chemical Engineering Journal, 221 (2013), 382-397.

II. **Temperature-programmed desorption studies of NOx over $Ag\text{-}Al_2O_3$ as lean NOx reduction catalyst**
Muhammad Mufti Azis, Hanna Härelind, Derek Creaser
Manuscript to be submitted for publication

My contribution to the publications

Paper I

I prepared the catalyst, performed flow reactor experiments, developed microkinetic model, interpreted the results together with my coworkers and was responsible for writing and submitting the paper.

Paper II

I partially prepared the catalyst, performed flow reactor experiments, interpreted the results together with my coworkers and was responsible for writing the manuscript.

Table of Contents

Nomenclature

Roman symbols	Description	Unit
A	mass and/or heat transfer area	m^2
Ai	preexponential factor	s^{-1}
C	concentration	$mol.m^{-3}$
cp	heat capacity	$J.mol^{-1}.K^{-1}$
d	channel diameter	m
D_a	axial dispersion coefficient	$m^2.s^{-1}$
D_{AB}	binary diffusivity	$m^2.s^{-1}$
$Deff$	effective diffusivity	$m^2.s^{-1}$
Ea	activation energy	$kJ.mol^{-1}$
F_{tot}	molar flow rate	$mol.s^{-1}$
f_D	tortuosity factor	-
ΔG_R	Gibbs free energy of overall gas reaction	$J.mol^{-1}$
h	convection heat transfer coefficient	$J.m^{-2}.K^{-1}$
ΔH	enthalpy change of elementary step	$J.mol^{-1}$
ΔH_R	enthalpy change of overall gas reaction	$J.mol^{-1}$
k	rate constant	s^{-1}
K	equilibrium constant	-
kc	mass transport coefficient	$m.s^{-1}$
L	reactor length	m
$\ln(\mathrm{kref})$	natural logarithmic of rate constant at reference temperature	$mol.s^{-1}.kg^{-1}$
m	mass of segmental solid material	kg
n	number of ideal tank-in-series	-
N	molar flux	$mol.m^{-2}.s^{-1}$
N_c	number of sites	$mol.kg^{-1}$
Pe	Peclet number	-
q	heat flux in segmental solid material	$J.m^{-2}.s^{-1}$

r	reaction rate	mol.s^{-1}.kg^{-1}
$range$	range for parameter scaling	-
R	gas constant	J.mol^{-1}.K^{-1}
SSE	sum of the squares of error	-
ΔS_R	entropy change of overall gas reaction	J.mol^{-1}.K^{-1}
t	time step	s
T	temperature	K
u	superficial gas velocity	m.s^{-1}
w	mass of segmental catalyst	kg
x	diffusion length	m
ΔX	thickness of segmental layer	m
ΔX_1	the first thickness of first washcoat layer	m
y	molar fraction	-
Δz	length of segmental tanks	m

Greek symbols	**Description**	**Unit**
β	fitted kinetic parameters	-
Γ	lumped mass transfer coefficient	m^3.s^{-1}
θ	fractional surface coverage	-
λ	heat conductivity of segmental washcoat	W.K^{-1}.m^{-1}
ν	stoichiometric coefficient	-
σ^2	variance of impulse response	-
τ	mean residence time	s
χ	stoichiometric coefficient of adsorbed species	-

Subscript	**Description**
b	backward reaction
f	forward reaction
g	gas
i	gas component index

j	reaction index
k	tank index
n	layer index
r	reactor
ref	reference condition
s	solid
$scaled$	scaled parameter
$surface$	washcoat surface
$unscaled$	unscaled parameter
w	surface component index
x	axis perpendicular to the gas bulk flow

1 Introduction

1.1 NOx emission abatement from lean-burn engine

Improvement of urban air quality is always an important environmental issue particularly with growing concern to create a sustainable society. Road transportation is a major contributor to urban air pollution and therefore regulations have been made in several countries to reduce emissions from road transportation such as the Clean Air Act in the US and European emission standard EURO [1]. The major air pollutants targeted in the regulations are CO, Nitrogen oxide (NOx), Hydrocarbon and particulate matter [2]. Since global warming is also an alarming concern nowadays, very recently CO_2 emissions from vehicles have also been regulated for light duty and heavy duty fleets [2].

NOx is an interesting and important chemical compound in air pollutants in which its occurrence in the atmosphere is due to exhaust gas produced in combustion engines which is the most common form of propulsion for vehicles [1]. Emission of NOx to the atmosphere has severe consequences. Firstly, NOx plays a crucial role in the acid deposition problem [3]. In the atmosphere, NO readily oxidizes to NO_2 (reddish brown gas) and some of the NO_2 will react further with water vapor to from nitric acid and cause acid deposition (acid rain) damaging trees, soils and lakes. Secondly, NO together with NO_2 are responsible for the formation of photochemical smog. Nitrogen oxides will react with sunlight and volatile organic compounds (VOC) to form air-borne particles and ground level ozone known as photochemical smog. Smog usually occurs in large cities with sunny and warm climates packed with heavy road traffic. Photochemical smog has also serious health effects as it may cause or exacerbate respiratory related diseases [1, 3].

Most Internal combustion engines (ICE) nowadays use fossil fuel and compressed air. Since air contains 79% of N_2, in a highly oxidative atmosphere N_2 can be converted to NOx that is harmful to the environment. Generally, there are three ways to form NOx during combustion [1]:

- Thermal NOx: the NOx is produced from equilibrium reactions between N_2 and O_2 at elevated temperature such as in an ICE. The NOx emissions from an ICE is primarily as NO. The mechanism of NO formation is described by the Zeldovich mechanism [1]:

$$O + N_2 \leftrightarrow NO + N \tag{1}$$

$$N + O_2 \leftrightarrow NO + O \tag{2}$$

$$N + OH \leftrightarrow NO + H \tag{3}$$

- Fuel NOx: The minor source of NOx in emissions originates from nitrogen bound to the fuel (like oil or coal). During combustion, nitrogen may ionize and form free radicals to form N_2 or NO.
- Prompt NOx: During the initial stage of combustion, atmospheric nitrogen can react with fragments of hydrocarbons from the fuel forming several intermediates like NH and CN species. Further oxidation of these species will produce NO. The abundance of prompt NOx is a subject of scientific debate and it is estimated that prompt NOx is less dominating.

In the late 70s, the commercial three way catalyst was introduced in the US and functioned effectively to reduce CO, hydrocarbon and NOx emissions in parallel from gasoline engines. In an ordinary gasoline engine, the ratio between the air and fuel is near stoichiometric conditions for complete combustion. In line with the demand to achieve better fuel efficiency, diesel engines or lean-burn engines will increasingly become the major type of combustion engine in the future. In a diesel engine or lean-burn engine, the O_2 supply (as air) is in excess with respect to the amount of fuel and this will result in improved power output with lower CO_2 emissions [2, 4]. However, the conventional three way catalyst does not function effectively to clean up the lean-burn exhaust, particularly NOx emissions. Therefore, a better designed vehicle emission abatement system must be implemented [4].

There are two broad methods to control NOx emissions from ICE: pollution prevention aiming to reduce NOx generation (primary technique) and post-combustion treatment aiming to reduce NOx emissions (secondary technique) [1]. In a primary technique, NOx generation in the

ICE is suppressed by decreasing combustion temperature and controlling the oxygen-fuel concentration. An example of a primary technique is Exhaust Gas Recirculation (EGR). Selective catalytic reduction is an example of a secondary NOx abatement method.

The catalytic aftertreatment system is a common method to abate vehicle emission from mobile sources. In a modern diesel engine, the catalytic aftertreatment system often consists of three main parts: diesel oxidation catalyst (DOC), diesel particulate filter (DPF) and NOx reduction catalyst as depicted in Figure 1. The main function of the DOC is to oxidize carbon containing gases and to oxidize NO to NO_2. In the following part, the DPF traps solid particulate matters and NO_2 produced upstream in the DOC can be used for passive regeneration of the DPF. Eventually, a NOx catalyst is installed to convert the existing NOx to N_2 before releasing it to the atmosphere.

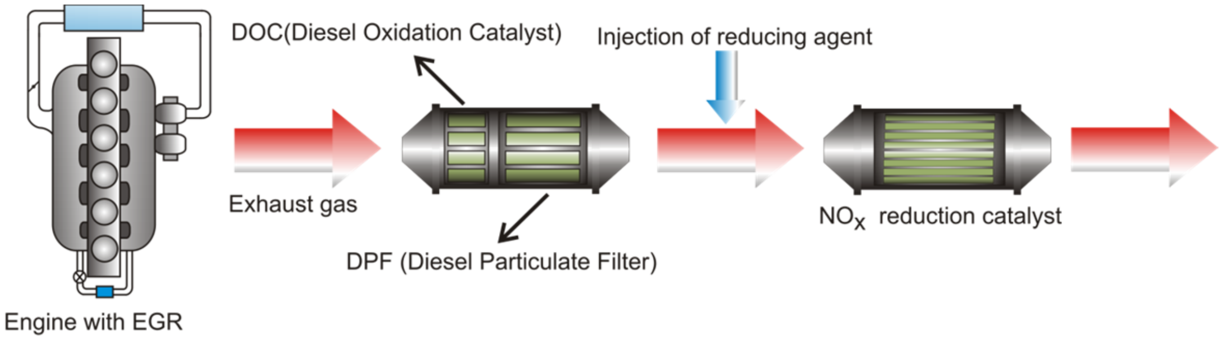

Figure 1. General schematic view of after treatment system in a lean-burn or diesel engine vehicle

For NOx reduction in a lean-burn system, Selective Catalytic Reduction (SCR) is a reliable method and has been widely installed in both mobile and stationary systems. With the SCR technique, the NOx is converted to N_2 with the aid of reductants. One way to do this is by using NH_3 (or urea solution) as the reducing agent, so called NH_3-SCR. Additional installation of a urea tank is needed onboard and it further requires an injection strategy to achieve better efficiency in NH_3 consumption.

Another technology to catalytically reduce NOx is the lean NOx trap (LNT) pioneered by Toyota which appeared on the market in 1994 [5]. Here, the NOx is stored on a catalyst (typically a

Barium based catalyst) under a lean period and followed by a short period (rich period) to regenerate the catalyst using a reducing agent. One of the challenges in LNT is deactivation by sulphur poisoning, where sulphur is converted to strongly bound sulphates and thus decreases the NOx storage capacity (as nitrates). Several attempts to improve the LNT technique have been discussed in literature [6]

The third concept of de-NOx technology in a lean-burn engine is hydrocarbon-SCR (HC-SCR). Here, the goal is to use the diesel fuel itself as a reducing agent and therefore installation of an additional tank for a reducing agent is not required. One of the potential catalysts for HC-SCR is silver alumina. Since HC-SCR over silver alumina catalysts will be the main focus of this thesis, it merits further discussion as presented in the following chapter.

1.2 Objectives

The overall goal of the project is to increase understanding of the reaction mechanism of HC-SCR over silver alumina catalysts. In this thesis, we have focused on the NO oxidation reaction as a starting-point for studying HC-SCR. Understanding the activation and formation of surface NOx species can be useful to elucidate the mechanism of HC-SCR over Ag-Al_2O_3. To achieve this, we initially developed a microkinetic model for H_2 assisted NO oxidation from transient experimental data. Subsequently, we conducted a series of TPD experiments to investigate the stability and characteristic of surface NOx species within the framework of HC-SCR. These findings may serve as an important basis to further understand the reaction mechanism of HC-SCR over Ag-Al_2O_3.

2 Hydrocarbon-Selective Catalytic Reduction (HC-SCR) over silver alumina catalyst

2.1 General

Early work on NOx removal in lean-burn or diesel engine exhaust conditions with hydrocarbon-SCR (HC-SCR) was pioneered by Iwamoto and Yahiro [7] and separate work by Held et al. [8] in the early 90s. Since then, numerous catalysts have been proposed and tested such as zeolitic based catalysts, platinum group metal (PGM) catalysts and several base metal oxides [9]. It appeared eventually that the two most promising candidates for HC-SCR are Cu-ZSM5 (typical maximum activity at high temperature region around 350°C) and Pt/Al_2O_3 (typical maximum activity at low temperature region around 250°C) [4]. However, challenges still remained since a significant amount of NOx is emitted in a temperature window between 250 and 350°C (quite common diesel exhaust temperature) which is not effectively covered by either Pt/Al_2O_3 or Cu-ZSM5. In addition, one shortcoming with Pt/Al_2O_3 as a HC-SCR catalyst is its significant selectivity for production of N_2O which is one of the detrimental greenhouse gases and hence its emission to the atmosphere must be minimized.

Cu-ZSM5 as an alternative candidate for a HC-SCR catalyst unfortunately also has some limitations. It has been reported in literature that Cu-ZSM5 suffers from poor hydrothermal durability, where the activity for NOx removal degrades in the presence of water vapor (real exhaust gas typically contains a H_2O concentration >10%) due to de-alumination of the zeolite framework at high temperature [4, 9]. Several attempts to augment the water resistance of zeolitic based materials have been reported [10, 11]. However, the main issue related to poor low temperature activity over Cu-ZSM5 has hindered further development of this catalyst as a HC-SCR catalyst.

2.2 Silver alumina for HC-SCR

There is considerable interest in developing HC-SCR catalysts with a high activity over a broad temperature window, good hydrothermal stability, sulphur tolerance, economically competitive as well as providing potential for a minimal fuel penalty. Silver alumina appears to be a promising candidate for HC-SCR application and has been widely investigated since the pioneering work by Miyadera in 1993 [12]. However, it is worth mentioning that silver alumina catalysts have poor performance in the low temperature region, until it was found that the addition of H_2 to the inlet feed gave a substantial increase in the low temperature activity [13, 14]. Since then, numerous studies have been devoted to investigate the role of H_2 and the reaction mechanism of H_2-assisted HC-SCR.

Silver alumina catalysts have been tested with various types of hydrocarbons (HC) i.e. short chain, long chain, aromatic, alcohol, biodiesel and real diesel fuel [15-21]. Tests with silver alumina have shown that reductants with a high carbon number were more superior than low carbon number reductants in terms of activity and tolerance to water. As the carbon number increases, the “mean bond energy” (the average of all C-H and C-C bond energies in a HC) decreases and therefore HC activation (a step in the HC-SCR process) will be accelerated [17]. The use of more complex HC reductants such as aromatics gave lower activity than straight HC as reported recently [18]. Furthermore, it has been suggested that the NOx removal efficiency is not only influenced by the structure of HC but also by the silver structure over the catalyst [18].

As a result of growing interest to use bio-based fuel in the transportation sector, the feasibility to use various bio-based fuels such as alcohol (methanol and ethanol), biodiesel and DME have also been widely investigated in the literature [15, 19, 21, 22]. Since the early work on silver alumina by Miyadera [12], it has been shown that oxygenated HC (such as ethanol) is easier to be partially oxidized than non-oxygenated straight chain HC. As a result, oxygenated HC gives higher NOx removal activity than non-oxygenated straight chain HC. Comparing the activity of low molecular weight alcohols, it appears that propanol and ethanol gave remarkably higher NOx removal activity compared to methanol [17, 23]. DME-SCR over Ag/Al_2O_3 has been tested by Tamm et al.[22] with relatively low NOx reduction activity similar to methanol-SCR. Erkfeldt et al.[15] and Arve et al.[19] have investigated several biodiesel fuels over a silver alumina catalyst and reported moderate NOx reduction activity above 300°C. It has been suggested that below 350°C, biodiesel may inhibit the NOx removal by hindering NO adsorption on the surface while above 350°C the oxidation rate is high thus activating $Ag\text{-}Al_2O_3$ for HC-SCR [19].

The knowledge on the role of active sites over Ag/Al_2O_3 as a NOx reduction catalyst is still unclear. Depending on the preparation method, several suggestions have been put forward mentioning the presence of metallic silver, oxidized silver, isolated ionic silver and silver aluminate [24, 25]. Furthermore, it has also been suggested that the role of small silver clusters (Ag_n^{δ}) is important [26]. Although the exact role of each possible silver site is still being investigated, it is generally accepted that metallic silver has an oxidizing function and is thus responsible for activation of HC and NOx. Small silver clusters and oxidized silver have been proposed to activate the NOx reduction activity by partially oxidizing the reductant and promoting surface nitrate formation. Shimizu and Satsuma have summarized various silver states as active sites in their review and references therein [17]. The proportion of small silver clusters and metallic silver depends much on the silver loading and preparation technique. With impregnation methods, high silver loading tends to produce more metallic silver while low silver loading gives a higher proportion of small clusters of silver [24]. Sol-gel methods produce catalysts containing small silver clusters and oxidized silver which are more finely distributed in the alumina matrix [27].

2.3 Mechanistic studies and H_2 effect

One of the most challenging parts in HC-SCR over Ag/Al_2O_3 catalysts is to understand the reaction mechanism of NOx reduction, which is particularly complicated by the nature of hydrocarbons used that contribute to the formation of a number of intermediates (both spectators and active intermediates) during reaction. Several literature reports have addressed mechanistic aspects of NOx reduction over Ag/Al_2O_3 [9, 17, 21, 26, 28].

A general schematic diagram of HC-SCR mechanism over Ag/Al_2O_3 is shown in Figure 2. Generally the first step of HC-SCR is activation of NO and HC by O_2. NO and O_2 will form NOx surface species (nitrates and nitrites). Strongly adsorbed nitrate is known to self-inhibit the NOx reduction at low temperature [23, 29]. For activation of HC, the O_2 partially oxidizes the HC to form oxygenated HC surface components. Although the formation of oxygenated HC is generally agreed to occur, however, the structure and role of oxygenated HC surface compounds remains a subject of debate in the literature. Different interpretations of HC intermediates can be due to a variety of experimental conditions [17]. In the subsequent part of the HC-SCR mechanism, the nitrogen containing species are expected to react with oxygenated HC surface species forming several surface intermediates where the major surface species are R-NO (nitroso species), R-ONO (nitrite species), R-NO_2(nitro species), R-CN (cyanide species), R-CNO(isocyanate species) and R-NH_2 (amine species) [28]. It is believed that cyanide, isocyanate and amines are the dominant routes to eventually form gaseous N_2 during the HC-SCR [30-32].

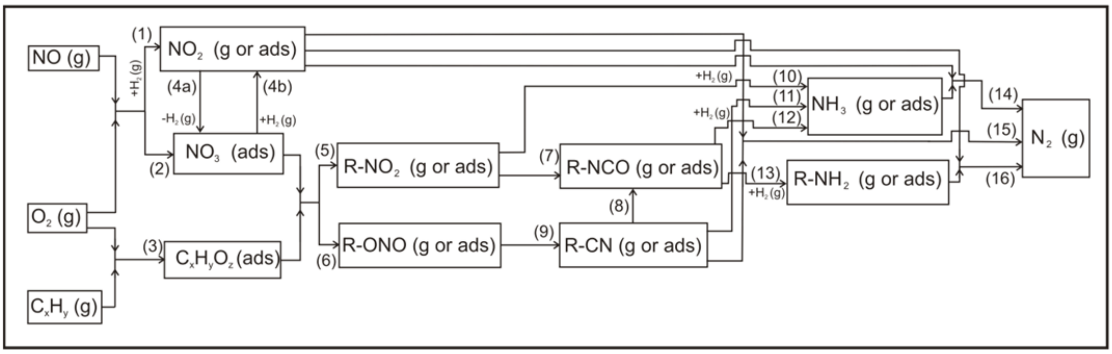

Figure 2. Schematic diagram of the reaction mechanism of H_2-assisted HC-SCR over Ag/Al_2O_3, adapted from [28, 33].

Perhaps, the most interesting feature of the silver alumina system for HC-SCR is the fact that the addition of small amounts of H_2 can strongly promote low temperature NOx reduction activity and therefore result in a wider temperature window for HC-SCR. Another catalyst that is promoted by H_2 for HC-SCR activity is Ag-MFI [34]. Defining the exact role of H_2 in HC-SCR over Ag/Al_2O_3 is far from trivial. From literature, there are several proposed explanations for the “H_2 effect” including:

- the enhancement of the partial oxidation of the reducing agent [28, 35].
- formation of reactive N species (like –NCO species [36] or gas phase radicals [28]) from the reducing agent.
- the accelerated formation of active cationic silver clusters [17, 26].
- the destabilization of surface nitrates blocking active silver sites [14, 35, 37-41]
- generation of Ag-hydride leading to formation of hydroperoxy radicals (HO_2), peroxide (O_2^{2-}) and superoxide ions (O_2^-) [26, 42].

It should also be considered that in a HC-SCR, it is possible that H_2 can have multiple roles among the effects mentioned above [14]. A recent study by Kim et al.[43] classified the roles of H_2 as *fast process* and *slow* process. The kinetic effect of H_2 was classified as a *fast process* in the time range of seconds. Here, H_2 activates formation of adsorbed surface species and chemical change of oxidized silver. Morphological changes such as the formation of silver clusters is classified as a *slow process* in the time scale of minutes.

It is important to mention that with addition of H_2, NH_3-SCR over Ag/Al_2O_3 was considerably promoted compared to in the absence of H_2 [44]. For this reason, the study of Ag/Al_2O_3 for HC-SCR and NH_3-SCR has also gained interest.

3 Experimental part

3.1 Catalyst preparation

Silver alumina powder was prepared by a freeze dried sol-gel method as described by Kannisto et al. [27]. Aluminium isopropoxide (98+%; Aldrich) was mixed with silver nitrate (>99.5%; VWR) in deionized water (milli-Q water). The silver loading used in this thesis was 5 wt.% (**paper I**)and 2 wt.% (**paper II**). To obtain a pH of around 4.5, 10 vol.% of nitric acid solution was added gently and than the solution was stirred overnight to form a transparent aluminum hydroxide sol.

Subsequently, the sol was placed in a round flask in a water bath to evaporate the solvent, i.e. isopropanol. This process was carried out under reduced pressure and a temperature of around 45°C. The evaporation process was ended when the sol became a transparent gel. The gel was then freezed with liquid N_2 and mounted onto a freeze dryer overnight. The resulting dry powder was then collected and crushed into a fine powder. The powder was placed in a ceramic crucible in a furnace for calcination. The calcination process was performed by first increasing the temperature at a rate of 2°C/min to reach 600°C and then holding it constant at 600°C for 6 h. Except for during calcination, the silver alumina was always protected by aluminium foil to prevent light exposure which can reduce the silver.

3.2 Coating of monolith with silver alumina powder

Bare cordierite monoliths (400 CPSI, 188 parallel channels with 1.1 mm open channel dimension) with 2 or 4 cm length and 2 cm diameter were used. Prior to coating, the bare monolith was calcined by the same procedure as used for the silver alumina powder. The silver alumina powder was mixed with boehmite (Disperal Sol P2; Condea) with the mass ratio of 4:1 and then mixed with milli-Q water under vigorous stirring. The monolith was coated by dropping the slurry uniformly onto the channels using non-graduated pipettes. The excess slurry was removed by blowing pressurized air gently through the channels. The coated monolith was dried under a hot air gun at 90°C for about 5 minutes and then briefly calcined at 600°C for 1-2 minutes. The monolith was then cooled down before it was weighed. The coating process was repeated until the targeted weight of washcoat was deposited. Afterwards, the coated monolith was calcined with a heating rate of 2°C/min to 600°C and held constant at 600°C for 3 h.

3.3 Flow reactor experiments

Flow reactor experiments were performed in a horizontal quartz tube (88 cm long and 2 cm diameter) heated by a helical heating coil on the outer surface of the tube. To prevent heat loss, the reactor was covered by quartz wool insulation. The monolith was placed inside the tube approximately 10 cm from the outlet end of the tube. To avoid bypass flow around the monolith, it was sealed inside the tube by a thin layer of quartz wool. To measure and regulate temperature, two themocouples (type K) were placed inside the sample. One was positioned at around 1 cm from the outlet end of the sample and the other one was inserted through the length of monolith until it protruded approximately 5 mm from the inlet end. The inlet temperature signal was controlled by a Eurotherm temperature controller. The inlet flow to the reactor was provided by several mass flow controllers (Bronkhorst Hi-Tech). Argon was used as a carrier gas. The total typical flow of inlet gas was 3500 mLn/min (1 Bar and room temperature), whereas in TPD experiments, a total flow of 1500 or 3500 mLn/min was used.

The reactor outlet gas composition was analyzed by a MKS 2000 FTIR instrument measuring the concentrations of NO, NO_2, H_2O, N_2O and NH_3 when HC was not fed. Additional measurements from aforementioned gases were made: CO, CO_2 and C_3H_6 when C_3H_6 (propene) was added. In some cases, a small part of the outlet flow from the reactor was sampled to a Hiden HPR 20 quadrupole mass spectrometer (MS) for gas analysis especially for diatomic gas measurements such as H_2, N_2, and O_2.

3.4 In-situ DRIFT spectroscopy

Diffuse Reflectance Infrared Fourier Transform Spectroscopy (DRIFT) is a useful in-situ technique to identify adsorbed surface species on a catalyst surface by detecting molecular vibration using mid-region infrared energy (wavenumber 200-4000 cm^{-1}) [45]. In DRIFT spectroscopy, an infrared (IR) source irradiates an IR beam which is reflected to enter the interior structure of a powder sample. The unabsorbed IR beam is transmitted to other particles or reflected out to a collecting mirror and sent to an IR beam detector for further analysis. A schematic diagram of DRIFT spectroscopy is depicted in Figure 3.

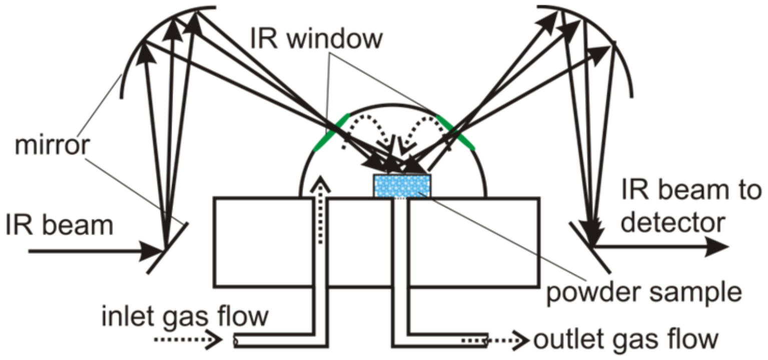

Figure 3. Schematic diagram of DRIFT Spectroscopy

The energy difference in vibrational states will characterize specific types of surface species. Adsorbed surface species on a catalyst will partially absorb IR photons and cause vibrations. However, only vibrations that trigger dipole moment changes can be detected with this technique [45]. The change of the dipole moment is proportional to the intensity of the IR band.

The DRIFT instrument used in this work was a Bio Rad FTS6000 spectrometer. One of the advantages of using DRIFT is the relatively simple operating procedure, where the analyzed sample can be mounted directly onto a DRIFT instrument for analysis. The powder sample was placed in a sample holder (supported by a metallic grid) of a Harrick Praying Mantis DRIFT cell equipped with a heating (up to 550°C) and cooling system. In addition, a thermocouple was placed near the sample holder to regulate the cell temperature. The gases were supplied by a number of mass flow controllers (Bronkhorst Hi-Tech). A fast switching valve is installed in the feed gas lines to allow a smooth step response during experiments. It is important to mention that a step response protocol is a common experimental technique in DRIFT to track the dynamic change of the absorbance peaks from surface species. The outlet gas from the DRIFT instrument is continuously sampled by a mass spectrometer (Balzer Quadstar 420) to facilitate gas analysis.

4 Kinetic modeling

4.1 General

The role of a kinetic model is to consolidate available experimental data with theoretical principles. It is hoped that a realistic kinetic model can capture the physical and chemical phenomena on the catalyst and hence it can give essential insights in the development of a catalyst. In a modern catalysis research cycle, development of a catalyst is not merely attributed to the knowledge of catalyst synthesis and surface science, but also uses kinetic modeling to elucidate the important steps in a reaction network (see Figure 4). According to Thybaut and Marin [46] , there are three interconnected aspects i.e. synthesis, performance and design are all important to create a successful catalyst for industrial applications. A better understanding of kinetic information will improve the synthesis and design aspects of the catalyst to obtain the best performance of a catalyst.

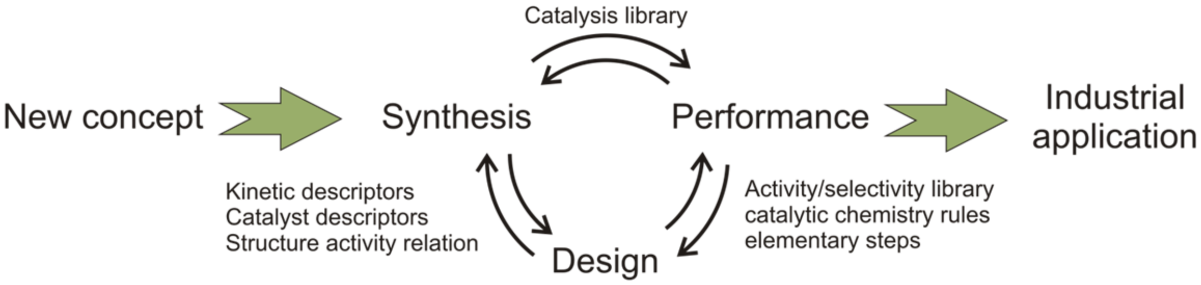

Figure 4. Schematic diagram of modern catalysis development. Adapted from [46]

4.2 Types of kinetic models

The level of kinetic modeling varies and generally can be classified as follow:

4.2.1 First principle modeling

First principle studies investigate how atoms react on a well defined surface. The rapid growth of computational technology has facilitated first principle studies based on quantum mechanics to give information about binding energies and electronic structures. The common method used nowadays is *Density Functional Theory (DFT)*. The results of DFT calculations can be useful to support detailed kinetic modeling studies to approximate reasonable limits of kinetic parameters (typically activation energies and preexponential factors). DFT modeling is not covered in this thesis and thus interested readers in DFT simulation studies over Ag/Al_2O_3 catalysts are referred to other literature [47].

4.2.2 Lumped kinetic modeling

Power law models are one of the simplest lumped kinetic models, based on the overall expression of a chemical reaction. Generally, a power law model can be written as:

$$r = \prod_{reactants} C^{\nu} \tag{4}$$

Power law models may be quite practical to use, especially for industrial applications. However, the applicability of the model is usually limited to a very narrow range of species concentrations, temperature and catalyst composition. Therefore, extrapolation to different catalysts and operating conditions is not very effective. A more detailed kinetic model needs to be employed, if one is interested in investigating reaction mechanisms.

A Global kinetic model is another type of lumped kinetic model that is used to describe heterogeneous catalytic reactions. Here, the description of the kinetic model considers adsorption, surface reaction and desorption steps of reacting species. An example of a common mechanism adopted in global kinetic modeling is Langmuir-Hinshelwood mechanisms where the adsorbed species react on the catalyst surface followed by desorption of products into the gas phase. Another mechanism available is Eley Rideal and Mars-Van-Kravelen. In an Eley Rideal mechanism, gas phase reactants may react directly with adsorbed species to form chemical reaction products as adsorbed species or gas phase species. In a Mars-Van-Kravelen mechanism, the catalyst surface experiences a redox cycle during chemical process.

In a global kinetic modeling, one way to resolve the kinetic rate expression is by assuming that one of the steps (can be adsorption, surface reaction or desorption) is the rate determining step and all remaining steps in quasi-equilibrium. Generally, kinetic rate expressions of global kinetic models can then be written as a function of gas phase properties as shown in equation (5) [46].

$$r = (kinetic\ factor) \cdot \frac{(driving - force\ group)}{(adsorption\ group)} \tag{5}$$

In the early work of catalytic aftertreatment processes in vehicles, an empirical global kinetic model was developed for NO, CO and hydrocarbon oxidation by Voltz [48]. This model is still widely used today, although often in somewhat expanded forms. It is noteworthy that one of the drawbacks of this method is the lack of physical interpretation of the kinetic parameters and therefore its range of predictability is limited [49]. Several challenges and limitations involved in obtaining a reliable kinetic model in automotive catalysis have been discussed by Olsson and Andersson [49]. For further assessment of kinetic analysis in heterogeneous catalysis, see a review by Lynggard et al.[50].

4.2.3 Microkinetic modeling

Microkinetic analysis is a tool to investigate the reaction mechanism over heterogeneous catalysis by assembling several elementary steps without pre-assuming that any step is the rate determining step or intermediate surface species most abundant [51]. Microkinetic analysis will typically generate a large number of elementary steps and form a highly correlated and non-linear mathematical system. Since a wide range of kinetic parameters may fit the experimental data, determination of kinetic parameters should be partially based on theoretical principles (physically and chemically sound) and other correlations to bridge the gap between the experimental data and the proposed microkinetic model.

A mean-field approximation is commonly used in a microkinetic model to describe the catalyst surface which assumes [52]:

a. distribution of particle size and shape are equal.

b. distribution of active sites is equal.

c. the distance effect between two different active sites is neglected and will be lumped within the effect of kinetic parameters.

d. adsorbed species are evenly distributed on the surface, i.e. islands of types of adsorbed species do not form.

By putting forward these assumptions, the probability for all active sites (i.e. neglecting differences between step and terrace sites) to adsorb gas phase reactants is considered equal. Microkinetic modeling with the mean-field approximation has been used in **paper I**. A more detailed work accounting for interaction of surface species on steps and terraces of active sites by using Monte Carlo simulations can e.g. be found in Olsson et al. [53].

In a microkinetic model, all elementary steps are described as reversible reactions and the rate of an elementary step as either a forward or backward reaction can be expressed as:

$$r_j = k_j \cdot \prod_{i=1}^{i=I} y_i^{\nu_i} \cdot \prod_{w=1}^{w=W} \theta_w^{\nu_w} \tag{6}$$

$$k_j = Ai_j \cdot \exp(\frac{-Ea_j}{R.T}) \tag{7}$$

From equation (6), it is noteworthy to mention that the order of the reaction with respect to gas phase or surface species concentration (ν) corresponds to the stoichiometry of the reaction. Preexponential factors and activation energies are the common kinetic parameters to estimate. In order to obtain reasonable kinetic parameter values, there are several strategies to determine kinetic parameters: investigating a sub-system from a larger system and determine the kinetic parameters independently, information from literature, thermodynamic restrictions, collision theory, transition state theory, statistical thermodynamics and finally from regression analysis with experimental data [6]. A combination of these methods can be used to obtain kinetic information from parameter estimation.

Estimation of preexponential factors for adsorption steps is generally taken from collision theory. The sticking coefficient at zero coverage is then fixed or estimated from literature values. For desorption and surface reaction steps, a reasonable limit for preexponential factors can be obtained from transition state theory [51].

Estimation of activation energies can be approximated from DFT calculation, bond-order conservation theory (BOC) or via the related but more advanced UBI-QEP (Unity Bond Index-Quadratic Exponential Potential) calculations and literature values [51]. Literature values of

UBI-QEP estimates have been used in **paper I** to estimate activation energies of desorption steps [54].

Thermodynamic restrictions based on overall gas phase reactions can also be applied in microkinetic modeling. Equilibrium of a chemical reaction is related to Gibbs free energy and its thermodynamic correlation can be written as:

$$\Delta G_R = \Delta H_R - T\Delta S_R = -R \cdot T \cdot \ln(K) \tag{8}$$

Rearranging equation 8 yields:

$$K = exp\left(\frac{\Delta S_R}{R}\right) \cdot exp\left(\frac{-\Delta H_R}{R \cdot T}\right) \tag{9}$$

The equilibrium constant, K, can also be expressed as a ratio between the rate constants of forward and backward reactions:

$$K = \frac{k_f}{k_b} = \frac{Ai_f}{Ai_b} \cdot exp(\frac{-(Ea_f - Ea_b)}{R \cdot T}) \tag{10}$$

Eventually thermodynamic restrictions for all elementary steps can be obtained by combining equation 9 and 10:

$$\prod_i (\frac{Ai_f}{Ai_b})^{\nu_i} = exp(\frac{\Delta S_R}{R}) \tag{11}$$

$$\Delta H_R = \sum_i \nu_i \cdot Ea_f - \sum_i \nu_i \cdot Ea_b \tag{12}$$

By implementing thermodynamic restrictions, one preexponential factor and one activation energy can be estimated for each overall reaction using equations 11 and 12. A more rigorous method to calculate thermodynamic consistency over a wide range of temperatures has been demonstrated by Mhadeshwar et al.[55]. Another concept of kinetic modeling for thermodynamic consistency is *"Thermodynamic state variable modeling"* by fitting the temperature dependent thermodynamic parameters (H and S) of the adsorbed species and transition states and using them in turn to estimate the kinetic parameters [52].

5 Reactor model: Single channel reactor model

5.1 General

Monolith-supported catalysts are the common form of catalysts used in the flow reactor facilities at the Competence Centrum for Catalysis (KCK) at Chalmers. For modeling purposes, the monolith catalyst or monolith reactor was simulated with a single channel reactor model as depicted in Figure 5a. This reactor model has been used in a microkinetic modeling investigation of H_2-assisted NO oxidation as demonstrated in **paper I**.

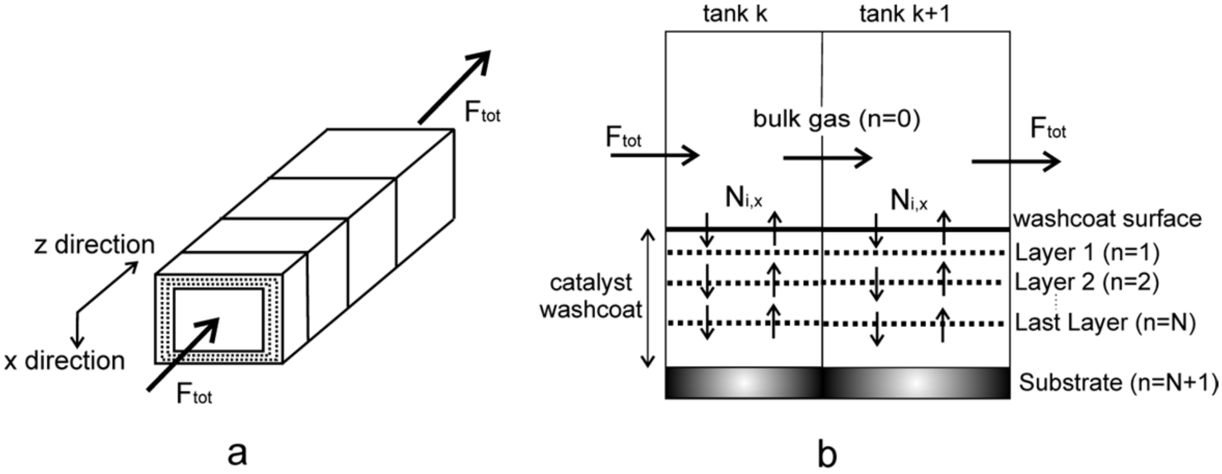

Figure 5. Single channel monolith model showing the washcoat discretization in axial (a) and radial direction (b) with arrows indicating mass transport.

As seen in Figure 5, the monolith reactor was modeled as tanks-in-series where the channel was segmented both in the axial and radial directions. By dividing the washcoat into several layers (Figure 5b), the reactor model is able to include internal mass transfer phenomena which is commonly excluded in a conventional kinetic model. In each tank and layer, mass and heat balance equations were solved for all gas and adsorbed surface species. The theoretical number of tanks required in the axial direction can be estimated using the dispersion model for laminar flow in an open-open system (equation 13-16) as described in [56]:

$$n = \frac{\tau^2}{\sigma^2} \tag{13}$$

$$D_a = D_{AB} + \frac{u^2 \cdot d^2}{192 \cdot \ D_{AB}} \tag{14}$$

$$Pe_r = \frac{u \cdot L}{D_a} \tag{15}$$

$$\frac{1}{n} = \frac{\sigma^2}{\tau^2} = \frac{2}{Pe_r} + \frac{8}{Pe_r^2} \tag{16}$$

The theoretical number of tanks-in-series (n) typically gives a large number of tanks and hence requires extensive computational time. Therefore, an alternative approach to estimate the number of tanks-in-series was employed by investigating the effect of varying the number of tanks and layers on the calculated sum of the squares of error (SSE). This approach is illustrated in Figure 6.

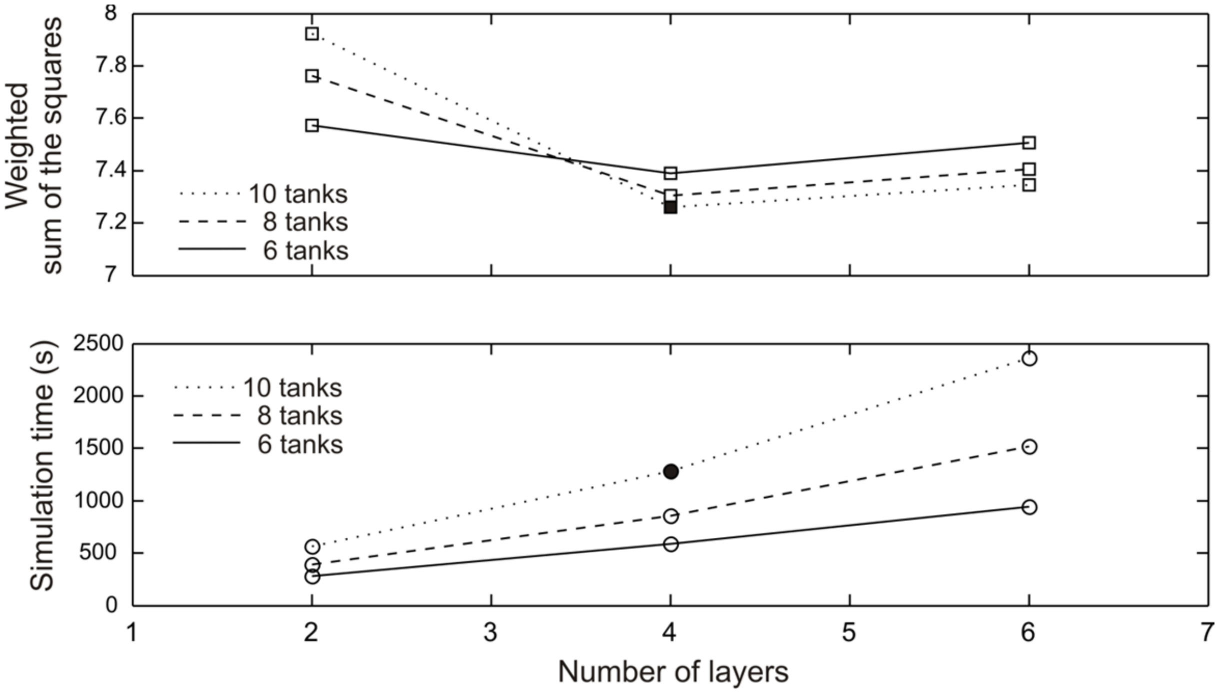

Figure 6. The effect of varying the number of tanks in series and number of layers on the weighted sum of the squares (top panel) and simulation time using standard desktop computer (lower panel). Filled symbols denote the simulation setup used in **paper I**.

As seen in Figure 6, varying the number of tanks and layers has affected the SSE. However, increasing the number of layers from 4 to 6 only changed the SSE about 1.5% and therefore it was concluded that 4 layers was sufficient to discretize the washcoat. From the lower panel of Figure 6, it can be seen that the time required for simulation increased monotonically with the increase of tanks and layers. From inspection of the gas concentration profiles, 10 tanks with an appropriate axial distribution were found able to well resolve the axial gas concentration. For simulation in **paper I**, 10 tanks and 4 layers has been used and it appeared to be sufficient to reach grid independence with reasonable computational time. It is also important to mention that the size of each tank (in axial direction) and layer (in radial direction) increased gradually to obtain a finer discretization where the concentration gradients were steeper. Figure 7 shows a schematic diagram of the washcoat depth and axial length discretization in the monolith reactor as layers and tanks respectively.

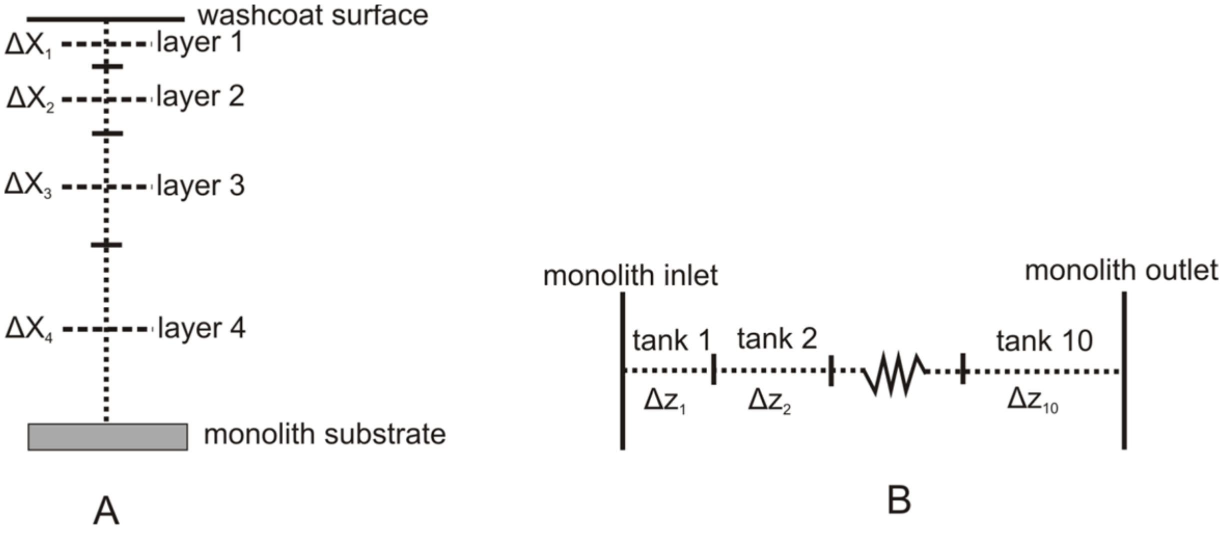

Figure 7. The schematic diagram of monolith reactor discretization: radial discretization in each tank (A) and axial discretization (B).

5.2 Modeling of mass and heat balances

The gas phase mass balance in each tank was modeled as a steady state mass balance between axial convective flow and radial mass transfer as shown in equation 17.

$$F_{tot} \cdot \left(y_{i,k-1,0} - y_{i,k,0}\right) - \Gamma_{i,k,0} \cdot \left(C_{i,k,0} - C_{i,k,1}\right) = 0 \tag{17}$$

The mass balance inside the washcoat is developed for each layer and characterized by radial diffusion (perpendicular to the bulk flow) and reactions. Equation 18 shows the mass balance in each layer (for layers n≥1)

$$\Gamma_{i,k,n-1} \cdot \left(C_{i,k,n-1} - C_{i,k,n}\right) - \Gamma_{i,k,n} \cdot \left(C_{i,k,n} - C_{i,k,n+1}\right) + \sum_j \nu_{i,j} \cdot r_{j,k,n} \cdot \mathrm{w}_{s,k,n} = 0 \tag{18}$$

The derivation of the overall mass transport coefficient (Γ) presented in equation 18 will be described in the following section.

A microkinetic model in this work was used to describe the transient simulations and therefore should be able to explain the dynamic change of surface species coverages. The dynamic mass balance of surface species is dictated by their involvement in reactions and expressed as:

$$N_c \cdot \frac{d\theta_{w,k,n}}{dt} = \sum_j \mathrm{r}_{j,k,n} \cdot \chi_{w,j} \tag{19}$$

The gas phase heat balance in each tank is assumed to be adiabatic and described as:

$$F_{tot} \cdot cp_g \cdot \left(T_{g,k-1} - T_{g,k}\right) - h_k \cdot A_k \cdot \left(T_{g,k} - T_{s,k}\right) = 0 \tag{20}$$

Accumulation terms in the mass balances (equations 17 and 18) and the gas phase heat balance (equation 20) were neglected because the characteristic time constants for these transport processes is considerably smaller compared to accumulation of surface (equation 19) species and heat in the solid (catalyst and washcoat).

For the heat balance in the washcoat, heat transfer in the radial direction within the washcoat was neglected. However, heat accumulation and transport between solid (washcoat and substrate) and gas in each tank was included. Also, axial heat conduction between solid segments and heat contribution from reactions in each tank were included. Equation 21 shows the segmental washcoat heat balance.

$$\frac{dT_{s,k}}{dt} \cdot cp_s \sum_n m_{s,k,n} = h_k A_k \left(T_{g,k} - T_{s,k}\right) - A_s \left(q_{k+1} - q_k\right) + \sum_n \sum_j r_{j,k,n} \cdot m_{s,k,n} \cdot \left(-\Delta H_j\right) \tag{21}$$

The solid heat flux for tank k, q_k, will be described in the following section.

5.3 Modeling mass and heat transport

A film model was applied to describe the mass and heat transport from the bulk gas to the washcoat. The values of kc and h varied along the axial direction of the channel according to the empirical correlation given by Hawthorne [57]. The molar flux $\left(N_{i,k,x}\right)$ of a gas component from the bulk-flow to the washcoat surface can be written as:

$$N_{i,k,x} = kc_{i,k} \cdot \left(C_{i,k,0} - C_{i,k,surface}\right) \tag{22}$$

The Molar flux $\left(N_{i,k,x}\right)$ of a gas component in the washcoat was explained by the Fickian mass transport equation. The general mass transport equation can be written as:

$$N_{i,k,x} = -Deff_i \cdot \frac{dC_i}{dx} + y_i \cdot \sum_{i=1}^{I} N_{i,k,x} \tag{23}$$

By assuming that equimolar counter-diffusion prevails due to the low species concentrations, the second term on the right hand side of equation 23 can be neglected which yields:

$$N_{i,k,x} = -Deff_{,i,k} \cdot \frac{C_{i,k,1} - C_{i,k,surface}}{0.5 \cdot \Delta X_1} \tag{24}$$

The effective washcoat diffusivity was calculated from the Bosanquet [58] correlation by including gas diffusivity, Knudsen diffusivity and f_D factor (accounting for porosity and tortuosity of the washcoat). Gas diffusivity was calculated from the Fuller-Schettlet-Gidding relationship [59] and corrected for the current segmental washcoat temperature while Knudsen diffusivity was approximated by using the semi-empirical Knudsen correlation [60].

By equalizing equation (22) and (24) and eliminating the gas concentration on washcoat surface ($C_{i,k,surface}$), the mass transfer from the gas bulk to the washcoat surface can be expressed as in equation 25. Here, the lumped mass transfer coefficient (Γ) is defined.

$$N_{i,k,x} \cdot A_k = \frac{A_k}{\frac{1}{kc_{i,k}} + \frac{0.5 \cdot \Delta X_1}{D_{eff,i,k}}} \left(C_{i,k,0} - C_{i,k,1}\right) = \Gamma_{i,k,0} \cdot \left(C_{i,k,0} - C_{i,k,1}\right) \tag{25}$$

Between all subsequent layers, the mass transfer coefficients are similar and can be defined as:

$$N_{i,k,x} \cdot A_k = \frac{A_k}{\frac{0.5 \cdot \Delta X_n}{D_{eff,i,k}} + \frac{0.5 \cdot \Delta X_{n+1}}{D_{eff,i,k}}} \left(C_{i,k,n} - C_{i,k,n+1}\right) = \Gamma_{i,k,n} \cdot \left(C_{i,k,n} - C_{i,k,n+1}\right) \tag{26}$$

However for the bottom layer N, $\Gamma_{i,k,N} = 0$, inferring no transport to the monolith substrate.

One of the contributors to the heat balance of the segmental washcoat is heat conduction between solid segments (substrate and washcoat) in the axial direction. The solid heat fluxes (q_k) for k=2,…,K-1,K were calculated from equation 27.

$$q_k = -\lambda_s \cdot \frac{T_{s,k} - T_{s,k-1}}{0.5\Delta z_k + 0.5\Delta z_{k-1}} \tag{27}$$

where $q_k = 0$ for k=1 and K+1

5.4 Matlab implementation: simulation and parameter estimation

The mass and energy balances (equations 17 to 21) were expanded for each gas phase component, surface component, tank and layer. The solution of these equations gives the concentrations of gas and surface components, gas and catalyst temperature in each layer and tank for each measurement time. The resulting differential and algebraic (DAE) equations were solved using the ODE15s function in Matlab R2008a® and the results were stored in a large multi-dimensional matrix.

Parameter fitting was performed using the lsqnonlin function in Matlab R2008a®. This function uses a gradient search method to perform non-linear regression. Prior to the fitting, each parameter was scaled according to:

$$\beta_{scaled} = \frac{\beta_{unscaled} - \beta_{initial\ value}}{range} \tag{28}$$

The scaling factor called $range$ was set so that a scaled parameter value of +1 approximately doubled the reaction rate from the initial parameter value and a scaled value of -1 corresponded to approximately half the reaction rate. Subsequently, the upper and lower bounds were determined in accordance with the scaled values. The objective of non-linear regression was to minimize the sum of the square of error (SSE) where the residuals were calculated from outlet gas measured and calculated mole fractions.

Parameter fitting with numerous parameters as exemplified in **paper I** is a challenging task. One way to assess the effect of a parameter on the prediction capability to the overall model is by performing a sensitivity analysis. This method was used and sensitivities were evaluated from small perturbations of each kinetic parameter

6 Microkinetic modeling of H_2-assisted NO oxidation

6.1 General

One approach to investigate a large and complex reaction mechanism as exemplified by HC-SCR over Ag/Al_2O_3 catalyst is to divide it into simpler subsystems. As a part of the HC-SCR reaction mechanism, NO oxidation to NO_2 has been investigated as an important sub-reaction within HC-SCR [25, 61, 62]. It is important to mention that Ag-Al_2O_3 is considered a poor catalyst for NO oxidation [25, 63], however the addition of H_2 dramatically improves its low temperature activity even with the presence or absence of H_2O in the feed [13, 25, 42, 64, 65]. Therefore, it is also probable that the mechanism by which H_2 promotes low temperature NO oxidation shares some common features with how H_2 promotes low temperature HC-SCR over Ag-Al_2O_3. We have chosen to examine a microkinetic model for NO oxidation based on the role of H_2 to remove self-inhibiting nitrate species on the surface. This mechanism is widely addressed in the literature and it can be represented with rather simple surface chemistry as demonstrated in **paper I** [66].

Table 1. The concentration and temperature levels in the DOE of NO oxidation

	NO (ppm)	O_2 (%)	NO_2 (ppm)	H_2 (%)	T (°C)
low	400	6	0	0	250
centre	600	7	50	0.1	325
high	800	8	100	0.2	400

We investigated the kinetic behavior of NO oxidation over silver alumina using transient data generated by a reduced factorial Design of Experiments (DOE). DOE has been found to be a useful method to investigate the influence of several controllable factors on some measurable effects. Here, the feed concentrations and feed temperature were varied systematically between low and high levels around a centre point condition. The experiments were performed in three batches with constant temperatures and transient switches in the feed concentrations of reactants. Table 1 shows the levels of concentrations and temperature used to study the kinetic behavior of NO oxidation.

6.2 Kinetic analysis

A Langmuir–Hinshelwood based reaction mechanism was used to model the oxidation of NO and H_2 involving 5 gas phase species: NO, O_2, NO_2, H_2 and H_2O. Besides, 6 surface components (NO*, O*, NO_2*, NO_3*, H* and OH*) were considered in addition to vacant sites (*). Molecular adsorption was used to characterize the adsorption of NO and NO_2, whereas dissociative adsorption was used for O_2, H_2 and H_2O [67, 68]. There were 5 reversible surface reactions in the reaction network which explained the formation or consumption of NO_2*, the inhibition effect by NO_3* and the effect of H*. In total there are 18 elementary steps used in the microkinetic model. It is important to mention that the reaction mechanism was also developed based on multi-linear regression analysis using the steady state results from DOE experiments.

Preexponential factors for adsorption steps of gas components were calculated from kinetic gas theory. The sticking coefficients of gas components were assumed to be 0.1 except for O_2 which was taken as 10^{-5}. The area of an active site was assumed to be 8.10^{-2} m^2/site. The activation energies for adsorption steps were assumed to be zero suggesting non-activated adsorption processes.

Preexponential factors for desorption steps of most gas components were assumed to be 10^{13} s^{-1} which is the common values estimated from transition-state-theory. Preexponential factors for O_2 were adopted from a TPD study in literature [69]. An initial estimate of the preexponential factor for NO desorption, 10^{16}, was used and tuned during regression analysis while desorption of NO_2, O_2, H_2 and H_2O were fixed.

Due to thermodynamic constraints, 4 kinetic parameters were calculated from thermodynamic restrictions based on the overall reactions of NO and H_2 oxidation. As a result, 13 kinetic parameters were fitted by non-linear regression. For modeling purposes, the rate constant which follows the Arrhenius expression (equation 7) needed to be modified to decouple the high correlation between preexponential factors and activation energies. As a result, the fitted parameters were logarithmic values of the rate constant ($\ln(\mathrm{kref})$) at the average experimental temperature (T_{ref}) and the activation energy (Ea) as shown as:

$$k_j = \exp\left(\ln(\mathrm{kref})_j - \frac{Ea_j}{R}\left(\frac{1}{T_{s,k}} - \frac{1}{T_{ref}}\right)\right) \tag{29}$$

Note that the $\ln(\mathrm{kref})$ and Ea have completely different orders of magnitude. As presented earlier in section 5.4, parameter scaling was implemented to give uniform weight of the effect of parameters on the residuals during regression. The list of all elementary steps, their rate constants and final kinetic parameter values is presented in table 2.

6.3 Results and discussion

The steady-state results from reduced factorial design experiments were analyzed by multi-linear regression (MLR) analysis. The current MLR model gave a coefficient of determination of 0.994 and the normalized coefficient plot including their 95% confidence intervals are shown in Figure 8.

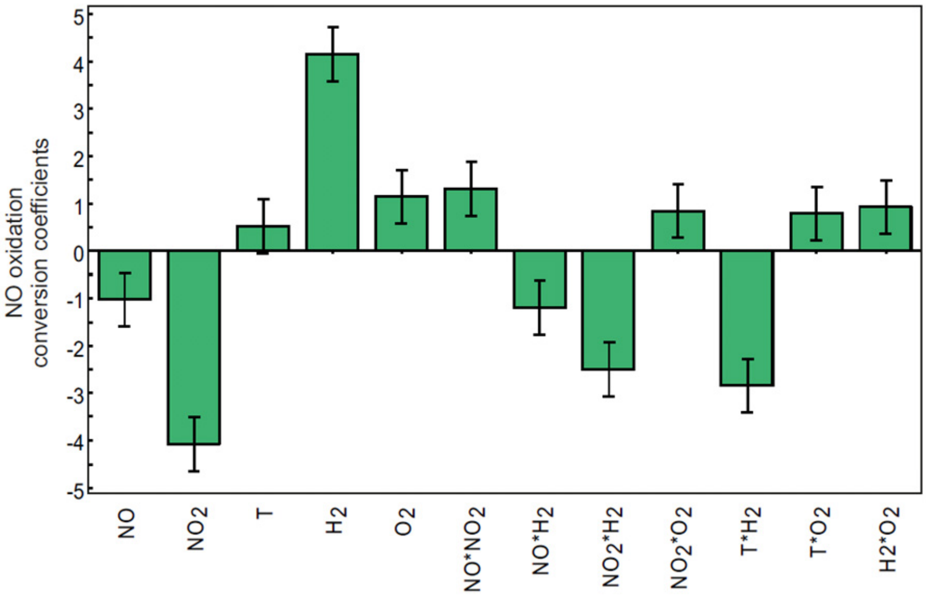

Figure 8. Normalized coefficient plots from MLR with 95% confidence interval bars

Table 2. The elementary steps used in the microkinetic model, the rate expressions and kinetic parameters

Forward reaction			*Reactions*	*Backward reaction*		
Ai (s^{-1})[†]	*Ea* (*kJ.mol*$^{-1}$)	*reaction rate* (s^{-1})		*reaction rate* (s^{-1})	*Ea* (*kJ.mol*$^{-1}$)	*Ai* (s^{-1})[†]
1.59×10^{7}	0.00	$r_1 = k_1.y_{NO(g)}.\theta_v$	$NO_{(g)} + * \Leftrightarrow NO*$	$r_2 = k_2.\theta_{NO}$	72	1.75×10^{17}
1.54×10^{3}	0.00	$r_3 = k_3.y_{O2(g)}.\theta_v^2$	$O_{2\,(g)} + 2* \Leftrightarrow 2O*$	$r_4 = k_4.\theta_O^2$	150.00	2.00×10^{12}
1.29×10^{7}	0.00	$r_5 = k_5.y_{NO2(g)}.\theta_v$	$NO_{2\,(g)} + * \Leftrightarrow NO_2*$	$r_6 = k_6.\theta_{NO2}$	53.13	1.00×10^{13}
6.15×10^{7}	0.00	$r_7 = k_7.y_{H2(g)}.\theta_v^2$	$H_{2\,(g)} + 2* \Leftrightarrow 2H*$	$r_8 = k_8.\theta_H^2$	20.00	1.00×10^{13}
2.06×10^{7}	0.00	$r_9 = k_9.y_{H2O(g)}.\theta_v^2$	$H_2O_{(g)} + 2* \Leftrightarrow OH* + H*$	$r_{10} = k_{10}.\theta_H.\theta_{OH}$	40.00	1.00×10^{13}
1.37×10^{13}	55.62	$r_{11} = k_{11}.\theta_{NO}.\theta_O$	$NO* + O* \Leftrightarrow NO_2* + *$	$r_{12} = k_{12}.\theta_{NO2}.\ \theta_v$	19.94	2.47×10^{8}
2.04×10^{14}	81.11	$r_{13} = k_{13}.\theta_{NO2}.\theta_O$	$NO_2* + O* \Leftrightarrow NO_3* + *$	$r_{14} = k_{14}.\theta_{NO3}.\ \theta_v$	114.98	1.10×10^{9}
1.00×10^{9}	36.51	$r_{15} = k_{15}.\theta_{NO3}.\theta_H$	$NO_3* + H* \Leftrightarrow NO_2* + OH*$	$r_{16} = k_{16}.\ \theta_{NO2}.\theta_{OH}$	152.77	2.12×10^{15}
1.62×10^{13}	103.43	$r_{17} = k_{17}.\theta_H.\theta_O$	$H* + O* \Leftrightarrow OH* + *$	$r_{18} = k_{18}.\theta_{OH}.\ \theta_v$	292.41	4.71×10^{11}

[†] *calculated from* ln(kref) *and Ea*

⬜ *=Fixed parameters*

🟩 *= constrained by thermodynamics*

🟦 *= estimated parameters*

The magnitude and trend of the coefficients were proportional to their effect on NO oxidation conversion. The detailed discussion of the MLR results can be found in **paper I**. In addition to individual variables, the MLR model also includes 7 selected interaction variables which have significant effects on the MLR model. However, evaluation of interaction effects cannot merely be interpreted from their coefficients in the overall MLR model, instead they were analyzed from the interaction plots of each pair (not shown here). The results from MLR analysis was also used to support the development of the reaction mechanism in the microkinetic model. Some important aspects from MLR analysis can be summarized as follow:

- H_2 clearly promoted the NO oxidation conversion as illustrated by its positive coefficient.
- The individual effects of NO and NO_2 were both negative on NO oxidation conversion. This can be rationalized by formation of self-inhibiting surface nitrates from NO and NO_2, since both are precursors to surface nitrates in the absence of HC.
- The interaction between T and H_2 ($T*H_2$) had opposite effects on NO oxidation conversion which indicates that increasing T in the presence of H_2 decreased the NO oxidation conversion while increasing T in the absence of H_2 increased the NO oxidation conversion.
- The $NO*H_2$ and NO_2*H_2 interactions had similar effects where increasing the NO or NO_2 concentration in the presence of H_2 tended to decrease the NO oxidation conversion. Without H_2, the effect of changing the NO or NO_2 concentration had a nearly negligible effect on the NO oxidation conversion.

An example of kinetic modeling results taken from a transient series at 400°C is shown in Figure 9. As seen here, the kinetic model used captured well the transient data of gas concentrations with correct trends and time-scale of responses. The activating role of H_2 by decreasing the surface nitrate coverage can be seen even at 400°C although this effect is not as high as at 250°C.

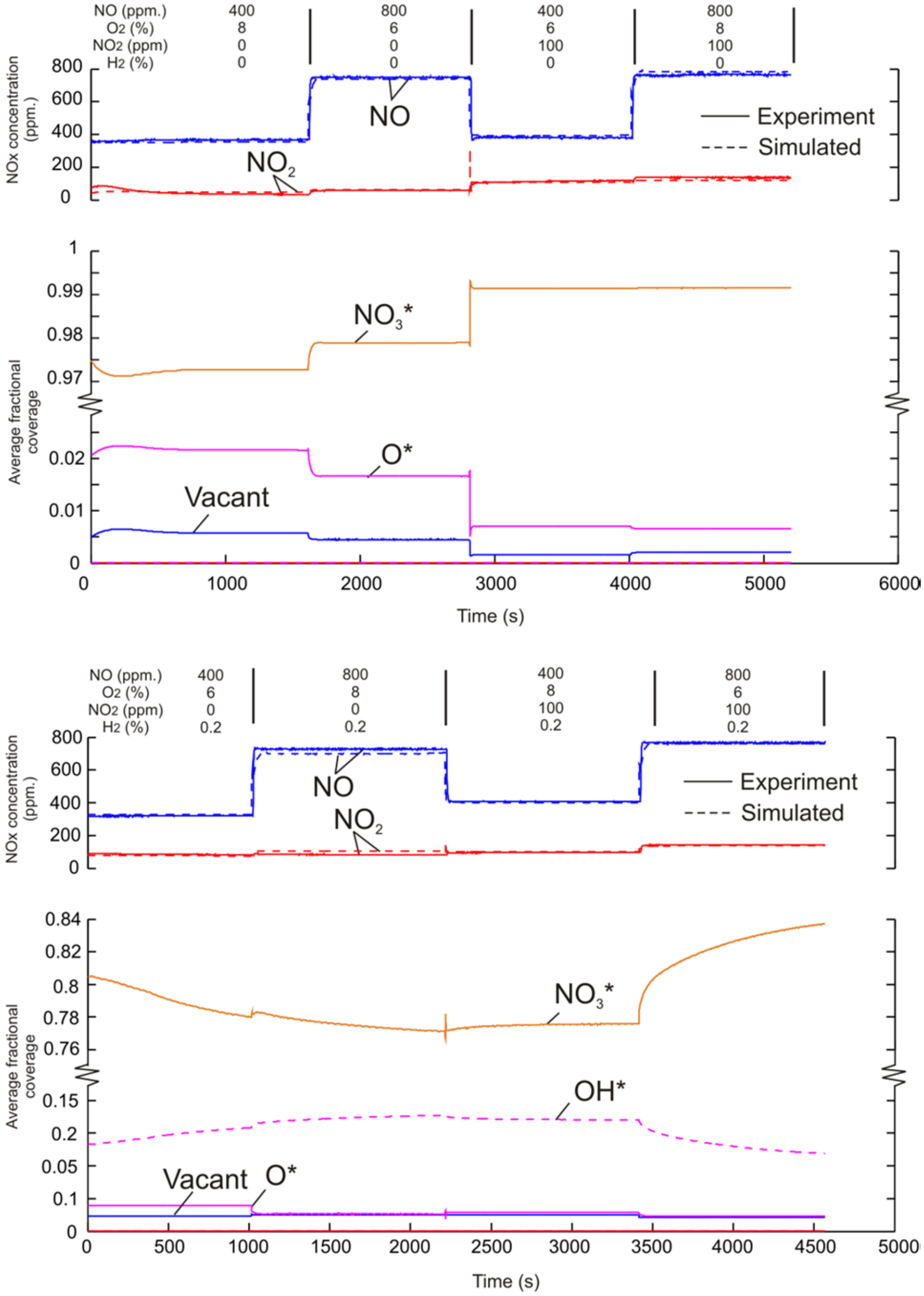

Figure 9. The experimental and simulation results from DOE experiment for varying feed concentration at 400°C.

Besides NO oxidation, H_2 oxidation to H_2O is an additional reaction that occurs when H_2 was fed. The nature of this reaction is fast and complete conversion of H_2 to H_2O was always observed already at 250°C which is also confirmed by the model. According to the model prediction of the H_2 concentration profile, the H_2 concentration decreased rapidly at the front part of monolith to form water due to its fast reaction. In addition, the model predictions as well as calculation of a Weisz modulus indicated the importance of internal transport limitations for diffusion of H_2 into the washcoat.

Instead of considering only the average surface coverage throughout the monolith, the current reactor model allows an analysis of the local surface coverage axially along the monolith as well as through the washcoat depth for each measurement time. In addition, the distribution profile of gaseous components both throughout the washcoat and axially through the gas phase can also be analyzed.

According to the modeling results, the enhancing effect of H_2 to reduce surface nitrate is isolated to a relatively small portion of the catalyst due to the fast reaction rate of H_2 oxidation (nearly 100% conversion for all experiments in this study) suggesting that internal transport resistance may play a role even for H_2 assisted HC-SCR with Ag-Al_2O_3. At high temperature, the effect of transport resistance is more prevalent causing the portion of the catalyst affected by H_2 to be even smaller. In the absence of H_2 in the feed, the gradient of nitrate coverage in the front part of monolith disappeared and the nitrate coverage became equal throughout the catalyst.

7 Stability of NOx surface species: in-situ DRIFT spectroscopy and TPD studies

7.1 Roles of surface NOx species

As seen in Figure 2, the reaction mechanism of HC-SCR over Ag/Al_2O_3 is initiated by activation of NOx and hydrocarbon (HC) by O_2. Activation of NOx is characterized by formation of surface NOx species mainly as nitrate and/or nitrite species. Subsequently, surface NOx species play a role by reacting with oxygenated HC (a result of HC activation) to form a number of intermediates which eventually lead to the formation of N_2. For this reason, surface NOx species have been suggested to be important intermediates and therefore it is important to understand their formation, stability and reactivity to elucidate the mechanism of HC-SCR.

It is interesting to note that H_2 may play a dual role in its interaction with nitrate species. On one hand, H_2 has been proposed to promote elimination of nitrates during H_2 assisted HC-SCR [33, 35, 38, 65]. On the other hand, it has also been shown that H_2 activates accumulation of nitrates on the surface, especially during NO oxidation [25, 35, 42, 61]. An additional objective for studying surface NOx species was to examine whether these seemingly contradictory roles for H_2 could be compatible.

Elimination of surface nitrates from the active silver species by H_2 has been proposed as one probable key step of the "H_2-effect" for low temperature HC-SCR [14, 33, 38, 65]. H_2 has been found to promote NO oxidation [13, 25, 42, 64, 65] and our previous study has simulated reaction steps 1,2 and 4 in Figure 2 to describe H_2-assisted NO oxidation [66]. It is important to mention that H_2 has been proposed to have several other roles in HC-SCR which has been discussed in section 2.3 and shown in Figure 2.

Contradictory to the hydrogen's proposed role to eliminate nitrates during HC-SCR, in-situ FTIR studies have been widely presented in the literature showing that H_2 plays an important role to activate the accumulation of surface nitrates following exposure of the catalyst to a NO-O_2-H_2 gas mixture [25, 35, 42, 61]. With the low silver loadings that are common for Ag/Al_2O_3

catalysts, it is also reasonable to expect that alumina also facilitates adsorption of surface NOx species. In addition, the existence of both silver nitrate and aluminium nitrate following NOx adsorption has been proposed [38, 70]. Unfortunately, in-situ IR analysis indicates overlapping peaks for nitrates over Ag/Al_2O_3 and bare Al_2O_3 which makes it difficult to discriminate between nitrates on the Al_2O_3 support and on the silver particles [42].

In order to investigate and clarify the characteristics and stability of nitrate species on Ag-Al_2O_3, we have conducted a DRIFT study and a series of TPD studies. The work presented in **paper II** was mainly based on the TPD studies of NOx adsorption over Ag-Al_2O_3 and Al_2O_3 where we have focused on understanding the role of H_2 to modify the surface NOx species in relation to the promotional effect of H_2 for NO oxidation and HC-SCR. Details regarding the experimental methods used can be found in **paper II**.

7.2 In-situ DRIFT Spectroscopy

Formation of surface NOx species was monitored by feeding 500 ppm NO and 8 % of O_2 at 100-400°C for 1 h (sufficient to reach steady states). The formation of nitrate species on the surface is depicted by Figure 10.

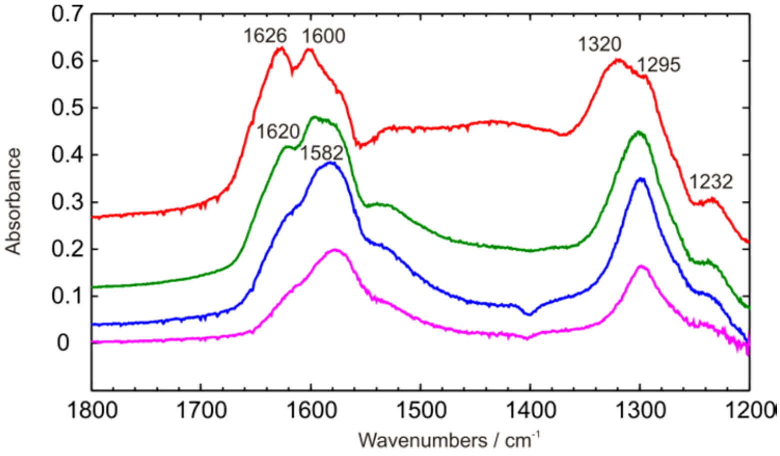

Figure 10. DRIFT results following 1 h adsorption of 0.1% NO and 8% O_2 over 5wt.% Ag-Al_2O_3 100°C (red), 200°C (green), 300°C (blue) and 400°C (magenta).

Assignment of nitrate species can be found from literature [71] to include: monodentate nitrate (1530-1480, 1290-1250), bidentate nitrate (1565-1500, 1300-1260) and bridging nitrate (1650-1600, 1225-1170). The presence of these three types of nitrate species is indicated by Figure 10.

In order to study their stability, periodical exposure to 0.1% H_2 pulses at 300°C were conducted with a 5 min. duration for each pulse. The results from the pulsing experiment are presented in Figure 11.

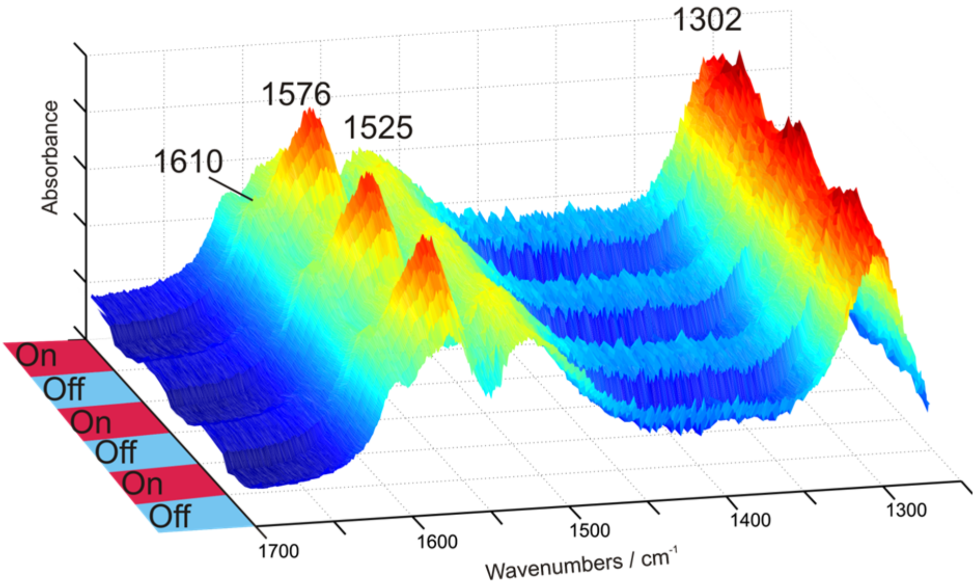

Figure 11. DRIFT results by pulsing 0.1% H_2 in (on) and out (off) of the feed stream at 300°C over 5 wt.% Ag-Al_2O_3. Alternating period is 5 min. Feed composition: 0.1% NO + 8% O_2 with Argon balance.

As seen from Figure 11, introduction of NO and O_2 gave assignable peaks to monodentate nitrate (1302, 1525), probably bidentate nitrate (1576) and bridging nitrate (1610). By pulsing 0.1% H_2, it is interesting to note that bidentate and bridging nitrate are the two most affected surface nitrate species. In a separate flow reactor experiment (not shown), it was found that the effect of H_2 on NO oxidation activity was fast and reversible giving higher NO_2 yield when H_2 was present and vice versa during its absence. Therefore, the DRIFT study as shown in Figure 11 has provided an interesting basis that led us to investigate further the stability and formation of surface NOx species over Ag-Al_2O_3 as presented in the following sections.

7.3 TPD studies of NOx

Temperature-programmed desorption (TPD) is a useful technique to investigate the thermal stability of adsorbed species. TPD studies to investigate the stability of surface NOx species over Ag/Al_2O_3 have been reported in the literature [23, 70, 72, 73]. In **paper II**, a series of TPD studies of NOx were carried out over Ag-Al_2O_3 and Al_2O_3 catalysts to quantify and characterize the stability of surface NOx species on the catalysts under reaction conditions for NO oxidation or HC-SCR. This study has also aimed to demonstrate the effect of H_2 to modify the quantities and types of surface NOx species, as it is well-known that H_2 promotes both NO oxidation and C_3H_6-SCR over a Ag-Al_2O_3 catalyst. We have focused our work on the low temperature region 200-300°C as it is expected to be favorable for nitrate formation and therefore most relevant to understand the "H_2 effect" for modification of nitrate species.

7.3.1 Nitrate formation following adsorption of NO-O_2, NO-O_2-H_2 and NO_2-O_2 gas mixtures over Ag-Al_2O_3 catalyst.

Figure 12 shows the adsorption and desorption profiles of NOx over Ag-Al_2O_3 for NO-O_2 (a,b), NO-O_2-H_2 (c,d) and NO_2-O_2 (e,f) gas mixtures. It was found that during the adsorption of NO-O_2 prior to the TPD (Figure 12a), the activity for NO oxidation was low however increased with higher temperature up to ca. 4% at 300°C. During the TPD temperature ramp that followed NO-O_2 exposure (Figure 12b), two desorption peaks were observed i.e. a low temperature (LT) peak at 277-340°C and a high temperature (HT) peak at ca. 440°C. It is noteworthy that the LT peaks were skewed to higher temperatures with increasing adsorption temperature. As seen from Figure 12b, the major NOx components desorbed were NO at both LT and HT peaks whereas NO_2 was only observed at the LT peak following adsorption at 200 and 250°C. The increase in NO oxidation conversion with increasing temperature was accompanied by a decrease in LT NOx desorption peak.

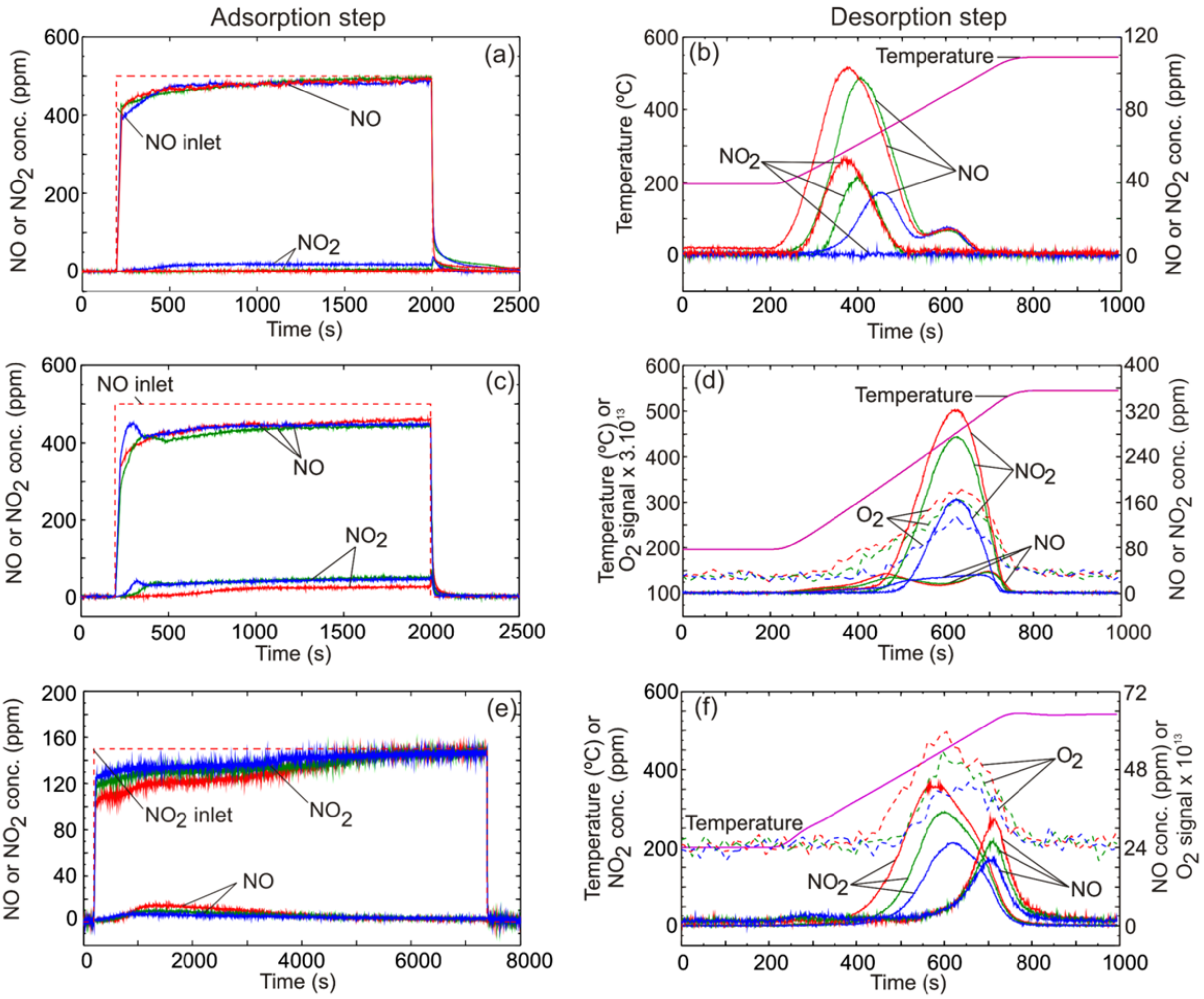

Figure 12. TPD following NO oxidation (a,b), H_2-assisted NO oxidation (c,d) and NO_2 adsorption (e,f) over Ag-Al_2O_3 at adsorption temperatures 200 (red), 250 (green) and 300°C (blue). Adsorption condition: 500 ppm NO + 4% O_2 total flow 1500 mLn/min (a), 500 ppm NO + 4% O_2 + 0.1% H_2 total flow 1500 mLn/min (c), 150 ppm NO_2 + 4% O_2 total flow 3500 mLn/min (e). Argon was used as carrier gas.

With addition of H_2, the NO oxidation conversion up to 10% at 300°C was reached during the adsorption step (Figure 12c). From Figure 12d, during the temperature ramp that followed adsorption of NO-O_2-H_2, a strong desorption peak of NO_2 was observed at ca.450°C which may be assigned as the HT peak and observed following NO-O_2 adsorption in Figure 12b. Desorption of O_2 (detected from m/z 16 from MS) was also observable and coincided well with the NO_2

peak. In addition, desorption of low concentrations of NO were observed at ca. 340-350°C and 505°C.

It can be noted that along with higher activity for NO oxidation in the presence of H_2, the LT peak observed from NO-O_2 TPD (Figure 12b) was significantly suppressed and shifted towards the HT peak (Figure 12d). The shift was also accompanied by higher total quantities of NOx adsorbed and desorbed. Due to the fact that the LT peak decomposed thermally at higher adsorption temperatures and was suppressed significantly in presence of H_2 which both gave higher NO oxidation conversion, it is therefore reasonable to assign the LT peak as resulting from decomposition of nitrates on the active sites.

Separate TPD studies of NO-O_2 and NO-O_2-H_2 over Al_2O_3 (not shown here, but available in **paper II**) did not give similar results, instead overall lower quantities of adsorbed NOx with neither a shift of the NOx desorption peaks nor promotion in NO oxidation activity with H_2 were observed. This suggested that the presence of Ag on Al_2O_3 was necessary in order for H_2 to interact and modify the adsorbed species.

Figure 12e shows the adsorption step of NO_2-O_2 TPD over Ag-Al_2O_3. As seen here, a temporary formation of NO could be detected during NO_2 adsorption. The quantities of NOx uptake decreased with higher adsorption temperature. It is noteworthy that the NO_2-O_2 system took much longer time to reach stable outlet NOx signals during the adsorption step compared to the NO-O_2 system due to the larger formation of surface NOx species on the catalyst.

Formation of NO was observable during the NO_2-O_2 adsorption over both Ag-Al_2O_3 and Al_2O_3. By integration of the curves in Figure 12e, the average ratio of total NO_2 uptake to total NO yield was 2.62 for Ag-Al_2O_3 and 3 for Al_2O_3. Therefore, one can formulate that self-oxidation of NO_2 was likely to dominate during the adsorption according to the following reaction:

$$2NO_2\,(g) \rightarrow NO_3(ads) + NO(g) \tag{30}$$

However also surface oxides were involved as in the following overall reaction [72]:

$$3NO_2(g) + O^{2-}(s) \rightarrow 2NO_3^-(ads) + NO(g) \qquad (31)$$

As seen from reactions (30) and (31), the ratio of NO_2 adsorbed and NO released is 2 in reaction (30) and 3 in reaction (31). The ratios from the integration results fit well and suggest that both reactions are likely occurring during NO_2-O_2 adsorption.

Figure 12f shows the desorption profile that followed adsorption of NO_2-O_2 over Ag-Al_2O_3. A substantial release of NO_2 was observed that peaked at 440-460°C. A minor desorption of NO was also detected at higher temperature ~525°C. It is important to mention that a broad release of O_2 was observed peaking at ~450-475°C.

TPD results for NO-O_2-H_2 (Figure 12d) and NO_2-O_2 (Figure 12f) were similar, giving a substantial release of NO_2 at a similar temperature range of the HT peaks. During the adsorption of NO-O_2-H_2, production of NO_2 was always observed and from comparison with Figure 12b and the low production of NO_2 during NO-O_2 adsorption, it is apparent that NO_2 production is linked to the formation of the HT nitrate. Further, additional experiments for NO_2-O_2 TPD on Al_2O_3 (not shown here but available in **paper II**) gave a similar TPD profile for the same adsorption conditions with Ag-Al_2O_3 (Figure 12f) suggesting that most of the HT nitrate formed is located on the Al_2O_3 support. Therefore, it was evident that the HT nitrate results from NO_2 adsorption and primarily located on the Al_2O_3 support. It is also then likely that the HT nitrates formed on the Al_2O_3 support are spectator surface species. From literature, a mechanism of NOx storage by a spillover mechanism has been proposed [38, 70]. An alternative mechanism of NOx storage by NO_2 readsorption on the Al_2O_3 support has also been proposed by Johnson II et al. [39]. Based on the results of these TPD studies, it is indicative that the NO_2 readsorption mechanism is most probable for NOx storage on Al_2O_3, since formation of the HT nitrate was related to the presence of gas phase NO_2. However, this does not totally negate the possibility for a spillover mechanism also contributing to NOx storage.

Additional studies on temperature-programmed reduction (TPR) were conducted to investigate the stability of nitrate species formed on Ag-Al_2O_3 and Al_2O_3. Upon introduction of H_2 during the desorption step that followed adsorption of NO-O_2-H_2 over Ag-Al_2O_3, the HT NOx desorption peak (Figure 12d) was shifted to significantly lower temperature (not shown here but available in **paper II**). Likewise, the shift of the HT NOx desorption peak was also observed for TPR that followed NO_2-O_2 adsorption over Ag-Al_2O_3. The shift of the NOx desorption peaks to lower temperature clearly occurred over Ag-Al_2O_3, but to little or no extent over Al_2O_3. Hence, these results infer the crucial role of Ag to activate H_2 which in turn can destabilize nitrate species. H_2 dissociation over Ag-Al_2O_3 itself has been proposed as an important initial step for H_2 activation in H_2-assisted HC-SCR [74].

7.3.2 Mechanistic insight regarding C_3H_6-SCR and H_2 assisted C_3H_6-SCR

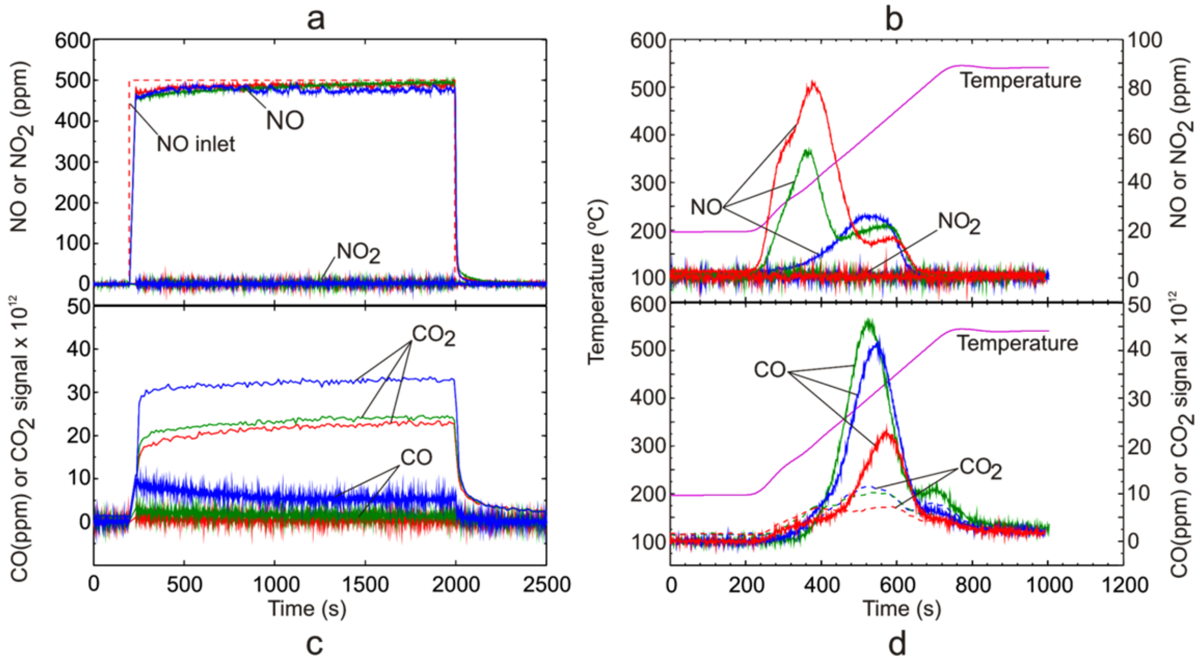

Figure 13. TPD following C_3H_6-SCR over Ag-Al_2O_3 showing adsorption (a) and desorption (b) of NOx, adsorption (c) and desorption (d) of COx. Adsorption conditions: 500 ppm NO + 4% O_2 + 0.1% C_3H_6 at adsorption temperatures 200 (red), 250 (green) and 300°C (blue). Total flow was 1500 mLn/min with Argon as carrier gas.

Further, a series of TPD studies were conducted to investigate the quantities and nature of adsorbed NOx and COx species during C_3H_6-SCR and H_2 assisted C_3H_6-SCR over the Ag-Al_2O_3 catalyst. Figure 13 presents the NOx and COx adsorption and desorption profiles for reactive adsorption of C_3H_6-SCR.

During the adsorption step with C_3H_6-SCR (Figure 13a and 13c), NOx reduction conversion increased with higher temperature accompanied by the highest C_3H_6 conversion at 300°C. As seen in Figure 13b, two remarkable NOx peaks could be observed at ca. 290°C (LT) and 420°C (HT). It should be noted that following C_3H_6-SCR adsorption at 200°C a shoulder on the NO peak at ca.235°C could be seen. The LT NOx desorption quantity decreased with higher adsorption temperature and became markedly suppressed at the adsorption temperature of 300°C.

It is interesting to note that by comparing the NOx desorption profile for C_3H_6-SCR (Figure 13b) and NO oxidation (Figure 12b), both of them have a similar profile with LT and HT NOx desorption peaks. However, for C_3H_6-SCR (Figure 13b) the NO_2 desorption is very low, probably due to the presence of adsorbed HC species that reduce the surface NOx species to NO during their decomposition and desorption. This presence of both LT and HT nitrates in approximately the same temperature range indicates that NO oxidation and C_3H_6-SCR share some mechanistic features.

As shown in Figure 13d, the CO desorption peak was observed between 405 to 426°C while the CO_2 desorption peak was broad with the same rise and decline as the CO profile. In addition, COx desorption which was observed during the temperature ramp was related to decomposition and oxidation of adsorbed HC and oxidized HC species. There tended to be more of these species at higher temperature along with greater NOx reduction activity, suggesting that they are important intermediate species. Removal of the LT inhibiting nitrate at higher temperature was likely to allow more formation of these intermediate species for the NOx reduction process [72].

In order to investigate the influence of H_2 on C_3H_6-SCR, 0.1% H_2 was added in the adsorption step and the desorption profile of NOx and COx are presented in Figure 14. During the adsorption step for H_2 assisted C_3H_6-SCR (Figure 14a and 14c), higher NOx reduction activity was observed, reaching up to ~23% at 300°C. As seen in Figure 14b, a small peak of NO at 240°C and broad desorption peaks reaching a maximum at ~440°C were observed, whereas NO_2 desorption was negligible. These NO peaks decreased with higher adsorption temperature. The total quantities of NOx desorbed are higher in the case of H_2 addition than in the absence of H_2 during C_3H_6-SCR (comparing Figure 14b and 13b).

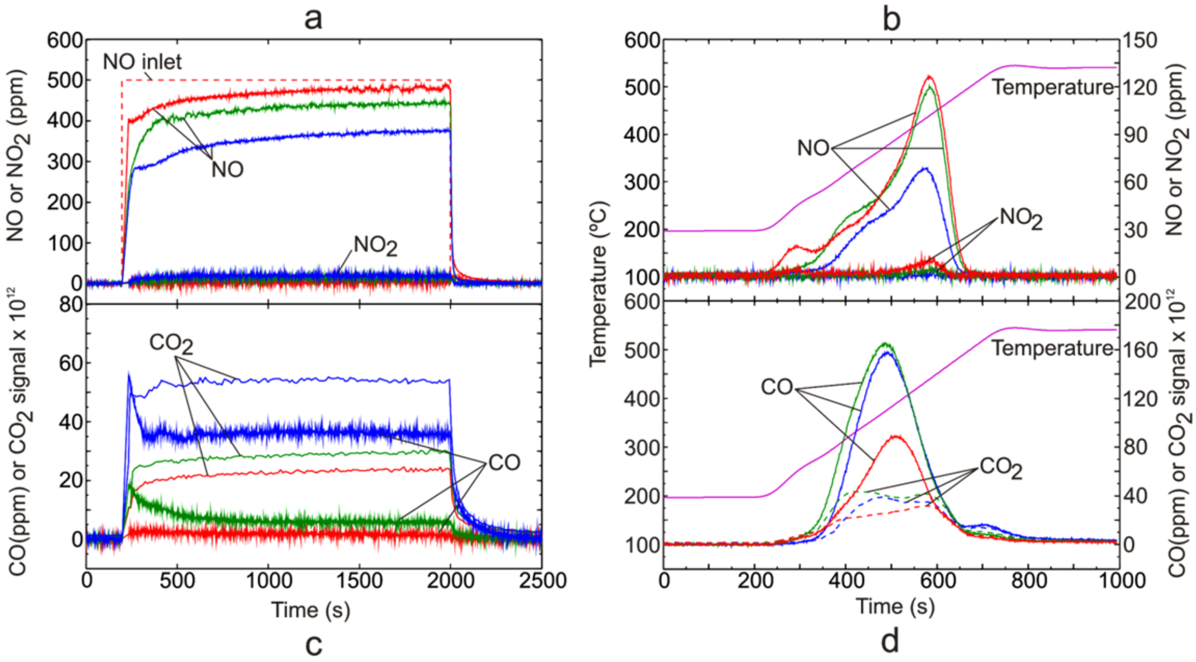

Figure 14. TPD following H_2 assisted C_3H_6-SCR over Ag-Al_2O_3 showing adsorption (a) and desorption (b) of NOx, adsorption (c) and desorption (d) of COx. Adsorption conditions: 500 ppm NO + 4% O_2 + 0.1% C_3H_6 + 0.1% H_2 at adsorption temperatures 200 (red), 250 (green) and 300°C (blue). Total flow was 1500 mLn/min with Argon as carrier gas.

The improvement in NOx reduction activity was also accompanied by a significant decrease in the LT NOx desorption peak as can be seen by comparing Figure 14b and 13b. At the same time, the HT NOx desorption peak increased remarkably. Therefore, again removal of the inhibiting LT nitrate, in this case aided by reaction with H_2, improved the NOx reduction activity. Unlike in the case of NO-O_2-H_2 (Figure 12d) and NO_2-O_2 (Figure 12f) TPD, the increase of the HT peak for H_2 assisted C_3H_6-SCR (Figure 14b) gave mostly NO desorption. The larger production of NO for H_2 assisted C_3H_6-SCR was probably because the catalyst also contained adsorbed HC which was oxidized by the adsorbed NOx species during their decomposition and desorption. From Figure 14b, it can also be seen that the HT nitrate peak had a broad shoulder towards lower temperatures. This shoulder probably results from the presence of the adsorbed HC species acting as reductants and destabilizing the nitrate species to cause some lower temperature NOx decomposition.

From the desorption profiles of CO and CO_2 (Figure 14d), one can see that a CO peak was observed at ca. 375°C which is at a lower temperature compared to the one in the absence of H_2 (between 405-426°C in Figure 13d). Furthermore, the concentration of COx released was much higher than in the absence of H_2, consistent with the higher conversion of C_3H_6 obtained with addition of H_2. Higher concentration of desorbed CO and CO_2 infers that H_2 has a promotional effect on low temperature C_3H_6 activation. HC activation to form oxidized HC species, itself is often suggested as a key step in HC-SCR over Ag-Al_2O_3 [35, 42]. This greater formation of surface HC and oxidized HC in the presence of H_2 is likely linked to the removal of inhibiting nitrate species as suggested by the suppression of the LT nitrates also with H_2. There was also a broadening and shift to lower temperature of the COx desorption peaks with the addition of H_2 (compare Figure 14d and 13d) which suggests that a greater quantity of possibly more reactive adsorbed HC species with lower thermal stabilities were formed. This perhaps points to the fact that H_2 may have other effects to promote the NOx reduction activity in addition to removal of inhibiting nitrate species.

It is noteworthy from Figure 13d and 14d that the concentration of CO during desorption did not monotonically increase or decrease with adsorption temperature, but instead peaked at adsorption temperature 250°C. Greater accumulation of adsorbed COx as temperature higher indicates that the reactions activating the HC and forming oxygenated HC on the surface have relatively high activation energies. In other words, the activation energy to partially oxidize HC to form oxygenated HC species is higher than the activation energy of subsequent reactions between surface NOx species with oxygenated HC species that lead to formation of N_2. Greater accumulation of oxygenated HC surface species may also be due to less inhibiting nitrates covering the active sites where oxygenated HC are formed.

In this series of studies, it seems that the promoting role of H_2 appears to be almost exclusively due to the removal of inhibiting nitrates, although it can be argued that the removal of these nitrates either thermally or by hydrogen reduction does not always result in a proportional increases in either NO oxidation or NOx reduction. As a result the findings here do not preclude the possibility of other H_2 promoting roles as already described in section 2.3. However an investigation of the merits of other roles for H_2 to promote NO oxidation or NOx reduction is beyond the scope of this study and the methods used here.

8 Conclusions and outlook

The overall focus of this work was to increase the understanding of the reaction mechanism of HC-SCR over Ag-Al_2O_3 catalysts and in particular the promotional effect of H_2. As seen in Figure 2, HC-SCR involves a number of reactions and intermediates. One approach to investigate a large and complex reaction mechanism is to divide it into simpler subsystems.

NO oxidation to NO_2 has been suggested as a subsystem within HC-SCR. **Paper I** focused on describing the promotional effect of H_2 on NO oxidation by its main role to remove strongly adsorbed nitrate species on the active sites. A combination of flow reactor experiments and microkinetic modeling were applied in **paper I**. A single type of active site was used to simplify the microkinetic model. A reaction network based on the Langmuir-Hinshelwood mechanism was proposed and it turned out that the modeling results could capture well the experimental results.

From microkinetic modeling results, it was found that H_2 was consumed rapidly in the front part of the monolith. The predicted concentration profiles of H_2 in the radial direction, through the catalyst washcoat, suggested that only a small proportion of the monolith was exposed to H_2. Complete conversion of H_2 was observed from experimental results. Therefore, it would be interesting to conduct further investigations to experimentally verify the existence of internal mass transport resistance effects.

Paper II demonstrated the role of H_2 to modify surface NOx species during NO oxidation and C_3H_6-SCR. Formations of two general groups of surface NOx species were found to be present: a less thermally stable group of so called “LT nitrates” and a more thermally stable group of “HT nitrates”. LT nitrate species were more likely related to the formation of inhibiting nitrate species on active sites. Feeding H_2 had been found to eliminate the LT nitrate and subsequently promote the NO oxidation and C_3H_6-SCR. In addition, the presence of H_2 also promoted the formation of a greater variety of adsorbed hydrocarbons. This points out that H_2 may cause other effects to promote C_3H_6-SCR over Ag-Al_2O_3.

It was also found that H_2 facilitated the formation of nitrate species on the Al_2O_3 support. It was also indicative that the mechanism of NOx storage on the Al_2O_3 support was mainly via NO_2 readsorption. From TPR studies, it was found that Ag also played an important role to activate H_2 and hence react with surface NOx species.

As continuation of this work, involving DRIFT-MS studies to relate the changes in surface species with gas phase can be a potential route to enhance understanding of the HC-SCR mechanism. Chansai et al.[36] have highlighted the importance of short time contact to be able to identify reactive surface species and minimize their interference from spectator surface species. Repeated fast cycling with H_2 pulsing has been carried out recently by Kim et al. [43] showing effects on the NOx conversion over two different time scales as a function of cycle time owing possibly to slow morphological changes in silver sites and other faster kinetic effects. Further clarification and verification by which H_2 modifies surface species formation, combined with morphological changes over Ag-Al_2O_3, can be an interesting topic to improve our understanding of HC-SCR.

By having all information from in-situ and flow reactor experiments, one could start thinking of assembling this entire puzzle into a kinetic model of full H_2 assisted HC-SCR system. The use of low chain HC or oxygenated HC can be an option to decrease the complexity of the studied system. However, even with a short chain HC one can end up with a large reaction network and many kinetic parameters, resulting in extensive computational time (see for example ref [75]). As an alternative, it would be interesting to start building a relatively affordable kinetic model to simulate the TPD data shown in **paper II** to involve the role of the Al_2O_3 support in a chemical reaction network. Another issue that is important in kinetic modeling is thermodynamic consistency. A relatively new concept namely “thermodynamic state variable modeling” can also be an interesting alternative as it primarily relies on bounded thermodynamic parameters to derive the kinetic parameters.

9 Acknowledgements

First and the foremost, I would like to thank God almighty as the One who gives me life. This work is financially supported by Swedish Energy Agency and Swedish Research Council. I would like to take this opportunity to express my sincere gratitude to the following people:

My heartfelt acknowledgement goes to Prof. Derek Creaser as my main supervisor. I highly appreciate your encouragement, constant support and inspiration to me. Thanks for giving me the opportunity to conduct PhD study at Chalmers and I am so lucky to have you as my supervisor.

My co-supervisor Assoc. Prof. Hanna Härelind from Competence Centrum for Catalysis (KCK) is greatly acknowledged for your constant support, invaluable input throughout my PhD research.

I would like to thank my examiner Prof. Bengt Andersson at the Division of Chemical Engineering. Special thanks to the head of division Prof. Louise Olsson in particular for good arrangement on my experiments. Prof. Claes Niklasson is greatly acknowledged for introducing me to Sweden and facilitated my master study at Chalmers several years ago. I also would like to thank Marianne Sognell for good administrative arrangement.

I would like to express my gratitude to Dr. Hannes Kannisto and Fredrik Gunnarsson for invaluable help in catalyst preparation. I also would like to thank Dr. Steffanie Tamm and Dr. Djamela Bounechada for your lab skills. Björn Lundberg is greatly acknowledged for practical help with Matlab. Special thanks to Silver-alumina members at KCK group for pleasant discussion and knowledge sharing.

My buddies Xavier Auvray and Dr. Stanislava Andonova, thanks for small and big things that we have shared together. I thank my past office mate Dr. Carolin Wang-Hansen and currently Dr. Chaoquan Hu for creating pleasant atmosphere in our office. Thanks to colleagues at the Division of Chemical Engineering and KCK Chalmers for pleasant working atmosphere.

Special thanks goes to Department of Chemical Engineering at Gadjah Mada University in Indonesia for always being cooperative. I would also like to thank Indonesian friends in Sweden for great friendship. You are my family here and living in Sweden would never be joyful without you.

In a more personal level, I would like to thank my families in Indonesia for endless pray and love to me. Special dedication to my late father, although you are not here you are always in my heart. Last but not least, my ultimate gratitude goes to my wife Afrina and my daughter Ghaisani for your true love and inspiration. Nothing is better than having both of you in my life.

10 Bibliography

[1] C.A.T. Center, Technical Bulletin: Nitrogen Oxides (NOx), Why and How They Are Controlled, US Environmental Protection Agency Research Triangle Park, NC, 1999.

[2] T. Johnson, SAE Int. J. Engines 4 (2011) 143-157.

[3] G.T. Miller, Living in the Environment: Principles, Connections and Solutions, Thomson Brooks/Cole, Toronto, Ontario Canada, 2007.

[4] R.M. Heck, Farrauto R. J., Gulati, S.T., Catalytic Air Pollution Control: commercial technology, John Wiley & Sons, Hoboken, N.J., 2009.

[5] S.i. Matsumoto, Catal. Today 29 (1996) 43-45.

[6] L. Olsson, Fundamental Studies of Catalytic NOx removal, Department of Chemical Reaction Engineering, Chalmers University of Technology, Gothenburg, 2002.

[7] M. Iwamoto, H. Yahiro, Catal. Today 22 (1994) 5-18.

[8] W. Held, A. König, T. Richter, L. Puppe, SAE Technical Publications Paper 900496 (1990).

[9] R. Burch, J.P. Breen, F.C. Meunier, Appl. Catal. B-Environ. 39 (2002) 283-303.

[10] Z. Chajar, P. Denton, F. Berthet de Bernard, M. Primet, H. Praliaud, Catal. Lett. 55 (1998) 217-222.

[11] H.-Y. Chen, W.M.H. Sachtler, Catal. Today 42 (1998) 73-83.

[12] T. Miyadera, Appl. Catal. B-Environ. 2 (1993) 199-205.

[13] S. Satokawa, Shibata,J., Shimizu, K.-i., Satsuma, A., Hattori, T., Appl. Catal. B-Environ. 42 (2003) 179-186.

[14] J.P. Breen, R. Burch, Top. Catal. 39 (2006) 53-58.

[15] S. Erkfeldt, A. Palmqvist, M. Petersson, Top. Catal. 54 (2011) 1219-1223.

[16] K.-i. Shimizu, A. Satsuma, T. Hattori, Appl. Catal. B-Environ. 25 (2000) 239-247.

[17] K.-i. Shimizu, A. Satsuma, Phys. Chem. Chem. Phys. 8 (2006) 2677-2695.

[18] H. Kannisto, K. Arve, T. Pingel, A. Hellman, H. Harelind, K. Eranen, E. Olsson, M. Skoglundh, D.Y. Murzin, Catal. Sci. Technol. 3 (2013) 644-653.

[19] K. Arve, J.R.H. Carucci, K. Eränen, A. Aho, D.Y. Murzin, Appl. Catal. B-Environ. 90 (2009) 603-612.

[20] V. Houel, P. Millington, R. Rajaram, A. Tsolakis, Appl. Catal. B-Environ. 77 (2007) 29-34.

[21] H. He, X.L. Zhang, Q. Wu, C.B. Zhang, Y.B. Yu, Catal. Surv. Asia 12 (2008) 38-55.

[22] S. Tamm, H. Ingelsten, M. Skoglundh, A.C. Palmqvist, Top. Catal. 52 (2009) 1813-1816.

[23] S. Kameoka, Y. Ukisu, T. Miyadera, Phys. Chem. Chem. Phys. 2 (2000) 367-372.

[24] N. Bogdanchikova, F.C. Meunier, M. Avalos-Borja, J.P. Breen, A. Pestryakov, Appl. Catal. B-Environ. 36 (2002) 287-297.

[25] S.T. Korhonen, A.M. Beale, M.A. Newton, B.M. Weckhuysen, J. Phys. Chem. C 115 (2011) 885-896.

[26] K.-i. Shimizu, K. Sawabe, A. Satsuma, Catal. Sci. Technol. 1 (2011) 331-341.

[27] H. Kannisto, H.H. Ingelsten, M. Skoglundh, J. Mol. Catal. A-Chem. 302 (2009) 86-96.

[28] K. Eränen, F. Klingstedt, K. Arve, L.E. Lindfors, D.Y. Murzin, J. Catal. 227 (2004) 328-343.

[29] M. Yamaguchi, I. Goto, Z.M. Wang, M. Kumagai, Stud. Surf. Sci. Catal. 121 (1999) 371-374.

[30] S. Chansai, R. Burch, C. Hardacre, J. Breen, F. Meunier, J. Catal. 276 (2010) 49-55.

[31] S. Kameoka, T. Chafik, Y. Ukisu, T. Miyadera, Catal. Lett. 55 (1998) 211-215.

[32] F. Thibault-Starzyk, E. Seguin, S. Thomas, M. Daturi, H. Arnolds, D.A. King, Science 324 (2009) 1048-1051.

[33] J.P. Breen, R. Burch, C. Hardacre, C.J. Hill, C. Rioche, J. Catal. 246 (2007) 1-9.

[34] J. Shibata, Y. Takada, A. Shichi, S. Satokawa, A. Satsuma, T. Hattori, J. Catal. 222 (2004) 368-376.

[35] J. Shibata, K.-i. Shimizu, S. Satokawa, A. Satsuma, T. Hattori, Phys. Chem. Chem. Phys. 5 (2003) 2154-2160.

[36] S. Chansai, R. Burch, C. Hardacre, J. Breen, F. Meunier, J. Catal. 281 (2011) 98-105.

[37] D. Creaser, H. Kannisto, J. Sjöblom, H.H. Ingelsten, Appl. Catal. B-Environ. 90 (2009) 18-28.

[38] R. Brosius, K. Arve, M.H. Groothaert, J.A. Martens, J. Catal. 231 (2005) 344-353.

[39] W.L. Johnson II, G.B. Fisher, T.J. Toops, Catal. Today 184 (2012) 166-177.

[40] K. Arve, H. Backman, F. Klingstedt, K. Eränen, D.Y. Murzin, Appl. Catal. A-Gen. 303 (2006) 96-102.

[41] H. Kannisto, H.H. Ingelsten, M. Skoglundh, Top. Catal. 52 (2009) 1817-1820.

[42] P. Sazama, L. Capek, H. Drobna, Z. Sobalik, J. Dedecek, K. Arve, B. Wichterlova, J. Catal. 232 (2005) 302-317.

[43] P.S. Kim, M.K. Kim, B.K. Cho, I.S. Nam, S.H. Oh, J. Catal. 301 (2013) 65-76.

[44] M. Richter, R. Fricke, R. Eckelt, Catal. Lett. 94 (2004) 115-118.

[45] J.W. Niemantsverdriet, Spectroscopy in catalysis: an introduction, Wiley-VCH Verlag GmbH & Co. KGaA, Weinheim, 2007.

[46] J.W. Thybaut, G.B. Marin, Kinetics of Catalyzed Reactions-Heterogeneous, in: I.T. Horváth (Ed.), Encyclopedia of Catalysis, John Wiley & Sons, Inc., 2010.

[47] S. Klacar, Chemical Properties of Oxidized Silver-A Density Functional Theory Study, Institutionen för teknisk fysik, Kemisk fysik, Kompetenscentrum katalys (KCK), Chalmers University of Technology, Gothenburg, 2011.

[48] S.E. Voltz, C.R. Morgan, D. Liederman, S.M. Jacob, Product R&D 12 (1973) 294-301.

[49] L. Olsson, B. Andersson, Top. Catal. 28 (2004) 89-98.

[50] H. Lynggaard, A. Andreasen, C. Stegelmann, P. Stoltze, Prog. Surf. Sci. 77 (2004) 71-137.

[51] J.A. Dumesic, D.F. Rudd, L.M. Aparicio, J.E. Rekoske, A.A. Treviño, The microkinetics of heterogeneous catalysis, ACS, Washington, D.C., 1993.

[52] J. Sjöblom, Parameter estimation in heterogeneous catalysis, Department of Chemical and Biological Engineering, Chalmers University of Technology, Gothenburg, 2009.

[53] L. Olsson, V.P. Zhdanov, B. Kasemo, Surf. Sci. 529 (2003) 338-348.

[54] A.B. Mhadeshwar, B.H. Winkler, B. Eiteneer, D. Hancu, Appl. Catal. B-Environ. 89 (2009) 229-238.

[55] A.B. Mhadeshwar, H. Wang, D.G. Vlachos, J. Phys. Chem. B 107 (2003) 12721-12733.

[56] H.S. Fogler, Chapter 14 in Elements of Chemical Reaction Engineering 4th edition ed., Prentice Hall PTR, Westford, 2006.

[57] R. Hawthorne, AIChE Symp. Ser. 70, 1974, p. 428.

[58] G.F. Froment, K.B. Bischoff, J. De Wilde, Chemical Reactor Analysis and Design 3rd edition, John Wiley & Sons, New York, 2010.

[59] E.N. Fuller, P.D. Schettler, J.C. Giddings, Ind. Eng. Chem. 58 (1966) 18-27.

[60] D.D. Do, Adsorption analysis: equilibria and kinetics, Imperial College Press, London, 1998.

[61] U. Bentrup, M. Richter, R. Fricke, Appl. Catal. B-Environ. 55 (2005) 213-220.

[62] J.H. Lee, S.J. Schmieg, S.H. Oh, Appl. Catal. A-Gen. 342 (2008) 78-86.

[63] F.C. Meunier, V. Zuzaniuk, J.P. Breen, M. Olsson, J.R.H. Ross, Catal. Today 59 (2000) 287-304.

[64] R. Burch, J.P. Breen, C.J. Hill, B. Krutzsch, B. Konrad, E. Jobson, L. Cider, K. Eränen, F. Klingstedt, L.E. Lindfors, Top. Catal. 30-31 (2004) 19-25.

[65] Y. Guo, J. Chen, H. Kameyama, Appl. Catal. A-Gen. 397 (2011) 163-170.

[66] M.M. Azis, H. Härelind, D. Creaser, Chem. Eng. J. 221 (2013) 382-397.

[67] H. Backman, K. Arve, F. Klingstedt, D.Y. Murzin, Appl. Catal. A-Gen. 304 (2006) 86-92.

[68] H. Backman, J. Jensén, F. Klingstedt, J. Wärnå, T. Salmi, D.Y. Murzin, Appl. Catal. A-Gen. 273 (2004) 303-307.

[69] G.W. Busser, O. Hinrichsen, M. Muhler, Catal. Lett. 79 (2002) 49-54.

[70] N. Sadokhina, D. Doronkin, P. Pributkov, V. Bukhtiyarov, R. Kvon, A. Stakheev, Top. Catal. 54 (2011) 1190-1196.

[71] H. Härelind, F. Gunnarsson, S.M.S. Vaghefi, M. Skoglundh, P.A. Carlsson, ACS Catal. 2 (2012) 1615-1623.

[72] Y. Guo, M. Sakurai, H. Kameyama, Appl. Catal. B-Environ. 79 (2008) 382-393.

[73] X. She, M. Flytzani-Stephanopoulos, J. Catal. 237 (2006) 79-93.

[74] S. Klacar, H. Grönbeck, Cat. Sci. Technol. 3 (2013) 183-190.

[75] B. Sawatmongkhon, A. Tsolakis, K. Theinnoi, A.P.E. York, P.J. Millington, R.R. Rajaram, Appl. Catal. B-Environ. 111-112 (2012) 165-177.